Chemical Geology 698 (2025) 123115

Contents lists available at ScienceDirect

Chemical Geology

journal homepage: www.elsevier.com/locate/chemgeo

Research Paper

Volatile loss during heating of lunar mare simulants and related compositions☆

Jennifer Sutherland [a,b,*], Kai-Uwe Hess [a], Thilo Bissbort [a,1], Simon Stapperfend [c], Axel Müller [d], Thomas C. Hansen [b], Alexander Rack [e], Donald B. Dingwell [a,f]

[a] Department of Earth and Environmental Sciences, Ludwig-Maximilians-Universität München, Theresienstraße 41, 80333 Munich, Germany
[b] Institut Laue-Langevin, 71 Avenue des Martyrs, CS 20156, 38042 Grenoble Cedex 9, France
[c] Chair of Space Technology, Technische Universität Berlin, Marchstraße 12-14, 10587 Berlin, Germany
[d] OHB System AG, Manfred-Fuchs-Straße 1, 82234 Weßling, Germany
[e] ESRF – European Synchrotron, 71 Avenue des Martyrs, CS40220, 38043 Grenoble Cedex 9, France
[f] GEOLAB, Zhongfa Campus, Beihang University, Hangzhou 311115, China

ARTICLE INFO

Editor: Claudia Romano

Keywords:
Evolved gas analysis
Flux
Neutron powder diffraction
Moon
Regolith
Simulants
Simultaneous thermal analysis
Volatiles

ABSTRACT

Due to the scarcity of returned lunar regolith samples, simulants are currently widely used for testing and validation of technologies destined for resource extraction and manipulation on the Moon's surface. Deductions about thermal processing parameters (such as temperature ranges associated with sintering and melting) and material properties rely on a close fidelity of the terrestrially-sourced simulant materials. To evaluate the degassing behaviour of lunar regolith simulants during heating and thereby inform the validity of comparisons to the behaviour expected of actual lunar regolith, we compare profiles via simultaneous differential scanning calorimetry (DSC), thermogravimetric analysis (TGA), and evolved gas analysis (EGA) across a range of designated mare simulants, freshly recovered volcanic samples, and synthesised lunar-like glasses. Simulants generally exhibit higher mass loss (related to volatile release at sub-solidus temperatures) than fresh volcanic material, though overlap is observed with one simulant (JSC-1A). Of the fresh sources, Etna ash most closely limits the anticipated water loss difference to original lunar soils to within one order of magnitude. Results from complementary neutron powder diffraction (NPD) indicate that a lowering of the melting onset due to volatile fluxing persists ca. 200–300 °C beyond the major degassing range in samples of several grams. The possibility to reduce the simulant fidelity gap through critical source selection and their inherent limitations are discussed, and refined pre-treatment recommendations are made.

1. Introduction

The volatile (H, He, C, N, O, F, S, Cl) contents of lunar regolith have far-reaching implications for scientific and exploration endeavours. Volatile sources are highly sought, both to constrain the early history of the Earth-Moon system, and to reduce launch mass and cost for return missions by way of extracting elements for propellant and life support consumables (Hurley et al., 2023). Although the post-Apollo consensus perceived regolith as almost devoid of indigenous water (Epstein and Taylor, 1973, 1974; Fegley and Swindle, 1993), re-evaluation at increased sensitivity and spectral reflectance data has overturned this notion. Within mare terrain, reported H_2O/OH abundances average up to around 500 ppm in the upper mm of large pyroclastic deposits, and reach 83 ppm H_2 (742 ppm water-equivalent hydrogen) to depths of tens of cm in KREEP (potassium, rare-earth elements, and phosphorous)-rich regions (Li and Milliken, 2017; Lawrence et al., 2022). Direct measurements of hydrogen concentrations in returned regolith components, however, indicate the trend: agglutinates > bulk soil > volcanic glasses (Saal et al., 2008; Liu et al., 2012; Hauri et al., 2015). These small concentrations belie their significance on melt behaviour and properties

☆ This article is part of a Special issue entitled: 'Silicate Melt Workshop' published in Chemical Geology.

* Corresponding author at: Department of Earth and Environmental Sciences, Ludwig-Maximilians-Universität München, Theresienstraße 41, 80333 Munich, Germany.
E-mail address: j.sutherland@lmu.de (J. Sutherland).
[1] Present address: Institute for Geology, Ruhr-University Bochum, Universitätsstraße 150, 44801 Bochum, Germany

https://doi.org/10.1016/j.chemgeo.2025.123115
Received 15 June 2025; Received in revised form 21 September 2025; Accepted 26 October 2025
Available online 30 October 2025

(e.g. Burnham, 1979; Dingwell et al., 1996; Dingwell, 1998); nowhere is this more evident than in explosive volcanic eruptions (La Spina et al., 2022). For that reason, excess volatiles harboured in weathered products are highly undesirable in terrestrial material that acts to approximate the lunar surface for validating thermal processing strategies leveraged by in situ resource utilisation (ISRU).

A suite of lunar regolith simulants has been developed by space agencies, industry, and academia to support widespread technology testing in the context of crewed Artemis and Chang'e programmes, whilst preserving the carefully curated Apollo collection. Simulants should match the mineralogy, particle size and morphology, and bulk density of genuine lunar regolith, though fidelity varies in view of their intended purpose (Taylor et al., 2016; Martin and Wagoner, 2022; Slabic et al., 2024). Requirements are most stringent for construction (e.g. Taylor and Meek, 2005; Taylor et al., 2018; Fateri et al., 2019; Caprio et al., 2020; Farries et al., 2021; Han et al., 2024) and chemical extraction (e.g. Reiss et al., 2020; Schlüter and Cowley, 2020; Guerrero-Gonzalez and Zabel, 2023) efforts involving heating. Different approaches rely on manipulating regolith via sintering (grain bonding via atomic diffusion and neck formation at contact points below the melting point of any constituent, unless assisted by a minor liquid phase (e.g. Wadsworth et al., 2022)), through partial or complete melting.

Pre-treatment strategies for engineered simulants aim to limit degassing and thermal decomposition effects driven by non-lunar phases, whilst maintaining aspects of morphological and mineralogical similarity. Conversely, missing solar wind components (H_2, He) are not accounted for. The issue of volatile-driven vesiculation has been discussed in the context of mechanical properties (strength, conductivity) and density reduction (Song et al., 2019; Lim et al., 2023). Efforts to quantify (Petkov et al., 2024) and attribute gas species to their respective sources (Street Jr. et al., 2010; Petkov and Voecks, 2023) pave the way for targeted heating to remove secondary minerals in order to replicate lunar characteristics at elevated temperatures more closely. These primarily focus on optimising the most widely referenced simulant, JSC-1A, which has been exposed to atmospheric weathering for ca. 20,000 years (Duffield et al., 2006). Listed strategies vary from those that apply temperatures of up to 750 °C and exploit different sample environments (John and Rogers, 2021; Wilkerson et al., 2023) – recognising heating rate, vacuum, and atmosphere are known to affect volatile release (Kotra et al., 1982) – to somewhat arbitrarily-defined temperatures, or none at all.

Evaluation of those pre-treatment efforts is notably detached from the original material it seeks to imitate. This disconnect is likely due to blanket approaches to maximise volatile-derived mass loss, compounded by a paucity of pyrolysis results on lunar samples with which to compare. Updated measurements at improved sensitivities have been encouraged; however, recent studies continue to encounter issues of contamination (Mortimer et al., 2015; Verchovsky et al., 2020a). Whilst calorimetric analysis of samples with different mineralogy has been considered (Morrison et al., 2019; Whittington and Parsapoor, 2022; Whittington et al., 2023), and the fluxing effect of gases alluded to (Street Jr. et al., 2010), a quantitative perspective on volatile significance for sintering and melting applications with a view to informing pre-treatment is absent. Furthermore, while most attention has been placed on corrective measures, comparatively little discussion has been devoted to the potential for fresher source material in the ongoing development of simulants. Such pristine compositions align with mare, rather than highland, analogues, which pertain to sites outside the immediate Artemis exploration zone (Shearer et al., 2020).

To compare the spread in simulant degassing fidelity and evaluate the potential for terrestrially-sourced improvements, we measured several evolved gases and collected simultaneous thermogravimetric and heat flow data for 15 simulants and freshly collected volcanic samples. We catalogue these features through to 1300 °C in Section 3. Melt onset for larger volumes of two simulants is further probed using neutron powder diffraction. In Section 4, we sequentially attribute the volatile loss origins and compare them against reported lunar abundances, before considering the impact of these differences on the as-yet undecided path(s) towards engineering of the Moon's surface.

2. Materials and method

2.1. Sample origins

2.1.1. Mare simulants

Six simulants are included in this study: (1) ESA-supported EAC-1A, obtained from basanite in the Siebengebirge Volcanic Field, Germany (Engelschiøn et al., 2020). (2) NASA-developed JSC-1A, mined from ash deposit related to Merriam Crater in the San Francisco Volcano Field, Arizona, USA (Ray et al., 2010). (3) Space Research Technologies' (formerly Exolith Lab) LMS-1 (second manufacture batch), comprised of 32.0 wt% Butler Arts basalt of undisclosed provenance (procured instead from Merriam Crater as of September 2023), mixed with 19.8 wt % GreenSpar anorthosite from Kangerlussuaq, Greenland, 32.8 wt% pyroxene (Stillwater Mine, Montana, USA), 11.1 wt% olivine (Sisters Mining District, Washington, USA), and 4.3 wt% unspecified commercial ilmenite (Long-Fox et al., 2023). (4) Off Planet Research's OPRL2N, also matched (90.0 wt%) to the San Francisco Volcano Field, with a further 10.0 wt% originating from the Shawmere Anorthosite Complex, Ontario, Canada (Off Planet Research, 2025). (5) OPRL2NT, a high-titanium version with 14.4 wt% ilmenite, reducing the mare component by a corresponding fraction. (6) TU Braunschweig's TUBS-M, now continued at TU Berlin, sourced from a basalt complex west of Göttingen, Germany (Linke et al., 2020). Our supply of JSC-1A is missing the finest grain fraction due to prior mechanical testing. Bulk chemistry data, where available, is reported in Table S1.

2.1.2. Volcanic deposits

Five of the six samples are recent volcanic products, collected shortly after eruption by members of the Department of Earth and Environment's volcanology group at LMU Munich. A lapillus sample from the August 2014 eruption of Mount Etna, Italy (approximately 20 mm in diameter), was collected by K.-U. Hess and subsequently crushed to powder. A reticulite sample from the 2018 lower East Rift Zone eruption of Kīlauea, Hawaii (ca. 50 mm in diameter), was collected by D.B. Dingwell. From this sample, two sub-samples were extracted: the outer glassy rind ('Kīlauea – outer') and an interior portion approximately 20 mm from the rim ('Kīlauea – inner'). An ash sample from the 2021 Cumbre Vieja eruption, La Palma, was collected by U. Küppers. The Krafla sample was collected from a 1984 basaltic lava flow in Iceland by F. Wadsworth. A portion of this sample showing no visible signs of alteration was crushed to powder. All samples were stored under ambient conditions.

Meteorologically-exposed Hawaiian ash from an area to the west of the visitor centre for the Mauna Kea observatories (nearby the cinder cone Pu'u Haiwahini) was supplied by J. C. Hamilton of the University of Hawai'i at Hilo. The site was used for three multi-agency analogue field campaigns on ISRU in 2008, 2010, and 2012, including testing of the Regolith and Environment Science, and Oxygen and Lunar Volatile Extraction (RESOLVE), and the Volatile Analysis by Pyrolysis of Regolith (VAPoR) instruments (e.g. ten Kate et al., 2013). The sieved tephra was dried in a commercial bakery oven at 177 °C (350 °F) for two hours as feedstock for the Precursor ISRU Lunar Oxygen Testbed (PILOT) demonstration (Clark et al., 2009) in 2008, and has been in storage ever since.

2.1.3. Processed analogue material

Synthesised 'green' and 'orange' glasses approximate the compositionally well-constrained pyroclastic beads first identified at Apollo 15 and 17 landing sites (Meyer, 2004, 2010). The glasses were prepared by mixing reagent-grade dried chemicals (Table S1) to match the corresponding lunar compositions. Oxide mixes totalling 100 g were loaded

into in Pt crucibles and melted at 1500 °C in a ZrO_2-lined $MoSi_2$-heated box furnace. The molten samples were then poured directly into Pt80Rh20 viscometry crucibles and subjected to high temperature viscometry to ensure homogeneity. Glasses were obtained post-viscometry by pouring the melts onto a water-cooled Cu plate. Reduced orange glass (Fig. S1) was generated by removing the viscometry crucible to a vertical gas-mixing tube furnace, where it was held and stirred for several days under a CO/CO_2 (18:2) gas mixture. The sample was manually removed from the base of the furnace and poured onto a steel plate.

A partially reduced version of the Mauna Kea sample was retained following the 2008 PILOT processing by Lockheed Martin (Clark et al., 2009). During that study, the ash was heated to ~900 °C for 90 min in a hydrogen reduction reactor to demonstrate low-yielding oxygen release from iron oxides.

2.2. Methods

2.2.1. Differential scanning calorimetry (DSC), thermogravimetric analysis (TGA), and evolved gas analysis by mass spectrometry (EGA-MS)

A Mettler Toledo TGA/DSC 3+ with high temperature furnace was used for simultaneous thermal analysis (STA). For each run, 25–125 mg of as-received regolith simulant or crushed natural material was measured (± 0.1 μg; ± 5 °C) in an alumina crucible and systematically corrected using reproducible baseline data conducted with empty crucibles. To synchronously identify released volatile species, the STA apparatus is linked to a ThermoStar Pfeiffer Vacuum GSD 320 EGA-MS via a transfer line heated at 150 °C to prevent gas condensation inside the capillary. An integrated vacuum pump generates a 10^{-9} bar environment to retrieve the gases from the STA furnace, ensuring a near-concurrent response and analysis of the targeted evolved species (ca. 1 s delay between STA and EGA-MS signals). A quadrupole separates the gases, which have been ionised by a filament, according to their mass-to-charge (m/z) ratio and trajectory stability within the applied oscillating electric fields. Arbitrary units are used for gas concentration as the signal pertains to ion current without direct physical interpretation. These values represent the relative fraction of targeted species and are not normalised to sample mass.

The analytical protocol is depicted in Fig. 1a. A purging and drying segment is initiated from room temperature (ca. 30 °C) to 150 °C at 2 °C/min to purge the furnace, remove adsorbed water from the sample, and stabilise the baseline gas concentration, using a 100 mL/min nitrogen (N_2 5.0, guaranteed purity of 99.999 %) flow. Next, the sample is heated from 150 °C to 1300 °C at 15 °C/min. This rate is a compromise based on returned volatile abundances: faster heating would increase the gas signal, improving detection sensitivity of low-abundance species, though dilute temperature resolution. At 1300 °C the sample undergoes a 10-min isothermal period, before cooling at 30 °C/min. Each analysis took ca. 200 min. Purging N_2 flow provided near-inert external conditions by displacing evolved gases and enabled the simultaneous detection of any H_2O, CO_2, SO_2, O_2, CH_4, or H_2S (extracted from unique m/z ratios of 18, 44, 64, 32, 16, and 34, respectively). Sensitivity is at 1 ppm level (10^{-14} A), except for H_2O and O_2, which is an order of magnitude greater owing to higher background in blank analyses. Empty baseline measurements indicate the supposedly inert N_2 atmosphere bears up to 200 ppm O_2, likely contributed by diffusion from the Teflon connection tube and ineffective purging. Owing to mass balance sensitivity, higher fidelity vacuum conditions could not be recreated, although Wilkerson et al. (2023) demonstrate similar mass loss evolution under vacuum ($< 10^{-4}$ mbar) and helium with JSC-1A. Furthermore, inert atmospheric conditions are more replicable in ongoing large-scale laboratory sintering and melting experiments.

Data are normalised to the mass at 150 °C to negate the effects of different storage conditions on adsorbed water quantity. Characteristic crystallisation (T_{Cx}, peak) and melting (T_{Mx}, onset) temperatures are identified, whereby the subscript x denotes distinct chronological events. The latter is constrained by the intersection of the inflectional tangent to the heating curve and the extrapolated slope of the endothermic melting baseline. Solidus ($T_{AS} = T_{M1}$) and liquidus (T_{AL}) temperatures are termed 'apparent', as at 15 °C/min they are expected to be an overestimation of the values at which samples attain thermal equilibrium. Furthermore, there may be residual crystalline phases that melt

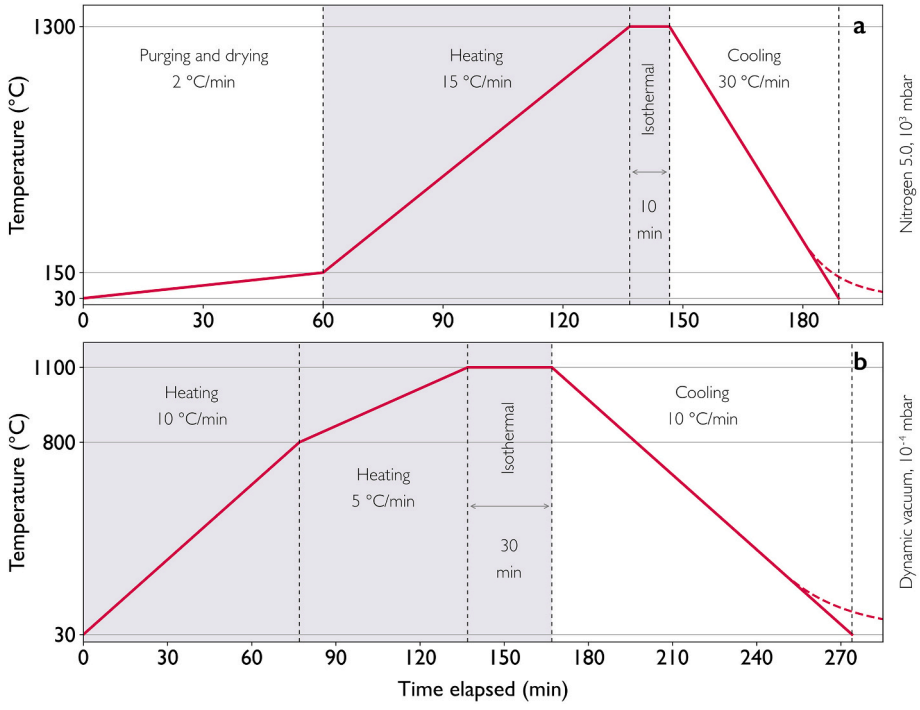

Fig. 1. Thermal protocols. Results herein correspond to the signals recorded during the heating and isothermal segments (shaded grey). (a) Simultaneous TGA-DSC and EGA. (b) NPD: slower heating and increased isothermal period owing to longer signal integration time and lower maximum temperature. In both cases, true sample temperature begins to appreciably deviate from the idealised profile below approximately 300 °C on cooling (dashed curve).

above 1300 °C. We refer to melt onset rather than maximum as a closer approximation of the intrinsic temperature at which the transition starts, less influenced by variations in sample mass, shape, density, and crucible contact. Where sample temperature is marginally elevated above the applied experimental limit (up to 1316 °C was recorded), the data has been plotted sequentially within the isothermal section, which may be interpreted as a minimum of 1300 °C. An experimental artefact expressed as a jump in the heat flow signal marks the transition from dynamic to isothermal heating. Strong fluctuation in mass loss rate around 150 °C is also an artefact from the shift in heating programme.

2.2.2. Neutron powder diffraction (NPD)

To examine the replicability of the DSC-derived melting onset and potentially attribute decomposition reactions, two simulants (JSC-1A and TUBS-M) with contrasting degrees of weathering were additionally probed using the D20 instrument at the Institut Laue-Langevin (ILL). Datasets are listed under Sutherland et al. (2021, 2024). JSC-1A represents an extensively referenced simulant, with a source material that provides a common basis for comparison across multiple simulant series. The selection of TUBS-M reflects the authors' involvement in a broader campaign to characterise this European-origin modular simulant system. To promote earlier melting, further measurements were taken after mixing TUBS-M with 30 wt% of a distinct, well-characterised (Jagota et al., 1990; Vasseur et al., 2016; Wadsworth et al., 2016, 2017) soda-lime glass (Spheriglass 2530, Potters Industries LLC, 45–90 μm).

A relatively long wavelength of 2.41 Å was prioritised over greater flux for high angular resolution ($\Delta 2\theta \sim 0.1°$) among densely clustered crystalline reflections. Individual patterns were integrated from the position sensitive detector ($0 < 2\theta < 150°$) over two minutes to improve counting statistics with a continuous temperature ramp. D20's dedicated dynamic vacuum furnace with a vanadium heating element imposed an upper limit of 1100 °C, although is sufficient to capture melt onset for basalt-like material (Chen et al., 2017; Giuliani et al., 2020). The nominal atmosphere at the pump decreases by three orders of magnitude to 10^{-4} mbar at the sample position in the furnace vessel. The thermocouples (± 5 °C) at the tip of the sample rod are ca. 3 cm from the neutron beam centre, and 1 cm above the sample surface. With one end at room temperature, the rod is a thermal bridge over ca. 60 cm, whose gradient likely lowers the recorded nominal temperature by an estimated 20 °C as compared to the temperature at the sample. This discrepancy has been accounted for in the display and interpretation of data.

The heating profile is highlighted in Fig. 1b. From room temperature the sample is raised to nominal 800 °C at 10 °C/min, which is then slowed to 5 °C/min from 800 until 1100 °C to better delimit phase changes approaching the melting interval. Each sample was held at 1100 °C for a further 30 min, before cooling at 10 °C/min. Vanadium cylinders (60 × 8 mm Ø) contained ca. 4 g of powder with 10 mm clearance and were loosely screwed with a vanadium cap to the sample rod. The attachment is not airtight, allowing evolved gases to be exchanged and removed via the furnace vessel. Neutrons permit larger sample volumes than X-ray alternatives, yielding a more representative bulk measurement for heterogenous samples. Destructive testing of several grams of genuine lunar regolith, however, will require more compelling justification when several mg may suffice for synchrotron usage. Pertinently, neutrons have greater sensitivity to light elements such as hydrogen, carbon, and oxygen due to their relatively large scattering cross-sections, making them an ideal probe of crystalline structures incorporating volatile components.

3. Results

3.1. TGA-DSC-EGA

3.1.1. Simulants

Characteristic temperatures and mass loss are presented in Table 1. Mass loss within the tabulated ranges is summarised in Fig. 2. CH_4 and H_2S were below detection limit for all runs. EAC-1A exhibits the highest mass loss of any sample (1.785 wt% total), with a prominent trimodal pattern peaking around 300, 550, and 750 °C (Fig. 3). Strong H_2O signals are recorded during all three, with the last preceded by a major two-step CO_2 release between 600 and 850 °C. SO_2 emerges as early as 500 °C and is most significant between 800 and 900 °C, with a smaller contribution after melt onset at 1072 °C. The melting interval, between apparent solidus (T_{AS}) and liquidus (T_{AL}), spans a 115 °C range. Neither an endothermic peak that could be related to a glass transition nor an exothermic peak related to crystallisation of glass is present in the DSC curves, indicating its absence or sub-detection levels in the as-received simulant.

By contrast, the basaltic cinder comprising JSC-1A is glass-rich (~30 wt% glass (Patridge et al., 2025)), enhanced in the missing fine grain (50 wt% <20 μm (Collins et al., 2022)) – resulting in a crystallisation peak (T_{C1}) at 824 °C. It demonstrates least alteration of all considered simulants at 0.161 wt% cumulative loss. Water content is about an order of magnitude less than EAC-1A, with two subtle contributions peaking around 300 and 650 °C, and almost exhausted by T_{C1}. The latter of these is associated with a pronounced CO_2 release. From 250 °C, very shallow oxidation is detectable through to ~1150 °C. The small upturn of the O_2 trace around 1300 °C is a persistent artefact accounted for by exact overlap of sample and background signals. The SO_2 signal following melt onset is comparable to EAC-1A; although spiked sources of SO_2 and CO_2 after T_{AL} are more prominent here, they remove little further mass. Among all simulants, no more than 9.3 % (JSC-1A) of the total cumulative mass loss is derived from the 1000–1300 °C range.

LMS-1 sustains consistently elevated water release up until approximately 1000 °C. No release of latent heat of crystallisation is observed, though glass is reported in the basaltic component (Long-Fox et al., 2023). Total mass loss is relatively high at 1.102 %. Three distinct contributions, from CO_2 then H_2O, are clustered between 650 and 900 °C. The middle of these is correlated with a subtle sharp oxidation at 770 °C; an earlier event is also detected centred on 460 °C. CO_2 release remains relatively far above the baseline through to the second melt onset (T_{M2}). Due to the considerable anorthosite fraction (19.8 %) and much later arrival of the apparent liquidus, the melting interval is comparatively drawn out over 210 °C.

OPRL2N crystallises expectedly close to JSC-1A (829 °C), given the basaltic cinder is derived from the same source. O_2 is, however, sharply consumed ~460 °C, in parallel with an additional release of CO_2 and H_2O. There is a further small inflection in the water profile between 900 and 1000 °C, presumably owing to the 10 % anorthosite substitution. For these two simulants only, the mass loss rate is not led by water release above 200 °C. SO_2 is more conspicuous following the onset of melting at 1049 °C (within 2 °C of JSC-1A); this is the latest emergence of SO_2 among all simulants, with a negligible share prior to T_{AS}. Like LMS-1, the anorthosite fraction pushes T_{AL} considerably higher (1225 °C, 63 °C above JSC-1A).

In the higher-Ti version OPRL2NT, where ilmenite partially substitutes basalt, mass loss is approximately doubled. This difference is primarily expressed by increased H_2O release under 600 °C, as well as a stronger CO_2 contribution in the 300–600 °C range. An additional decomposition around 940 °C simultaneously releases H_2O, CO_2, and SO_2. There is no distinct oxidation event as in OPRL2N, but a baseline discrepancy persists from ~260–1200 °C. T_{C1} is identical to the former. Post-liquidus CO_2 bubbling is the most pronounced of any simulant. Although the anorthosite content remains consistent with OPRL2N, T_{AL} is lower by 55 °C.

TUBS-M displays a prominent H_2O peak at 240 °C, such that the degassing profile is heavily skewed towards lower temperatures (81 % of the total mass loss is under 500 °C). Nearly all 0.797 wt% lost in this range is attributable to water. The relative CO_2 contribution, meanwhile, is the lowest of all simulants considered. From 600 °C evolved H_2O remains minor, aside from a small event at 750 °C overlapping a

Table 1
Temperature estimations (all in °C to the nearest integer) of key thermal events (± 5 °C) identified by DSC and mass loss contributions (3 d.p.) normalised to the dried sample mass at 150 °C. Crystallisation peaks (T_{Cx}), apparent solidus ($T_{AS} = T_{M1}$), distinct melting onsets (T_{Mx}), and apparent liquidus (T_{AL}) correspond to labels in Figs. 3–5. Mass loss ranges refer to sample temperatures, except for the applied 1300 °C upper limit, where the maximum sample temperature varies.

	Crystallisation T_{C1}	Crystallisation T_{C2}	Apparent solidus T_{AS}	Melting onset T_{M2}	Melting onset T_{M3}	Apparent liquidus T_{AL}	-Δwt% 150–500 °C	-Δwt% 500–1000 °C	-Δwt% 1000–1300 °C 10′ (% of total -Δwt%)	-Δwt% 150 °C -T_{AS}	-Δwt% T_{AS} - 1300 °C 10’	-Δwt% 150–1300 °C 10’
Simulants												
EAC-1A	–	–	1072	1157	1168	1187	0.681	1.042	0.0611 (3.42 %)	1.743	0.042	1.785
JSC-1A	824	–	1051	1138	–	1162	0.072	0.074	0.015 (9.32 %)	0.150	0.011	0.161
LMS-1	–	–	1035	1193	1223	1245	0.315	0.751	0.036 (3.27 %)	1.074	0.028	1.102
OPRL2N	829	–	1049	1139	1175	1225	0.103	0.212	0.017 (5.14 %)	0.320	0.011	0.331
OPRL2NT	829	–	1066	1138	1155	1170	0.373	0.271	0.026 (3.88 %)	0.652	0.018	0.670
TUBS-M	–	–	1161	1181	–	1196	0.797	0.169	0.012 (1.23 %)	0.978	0.001	0.979
Volcanic deposits												
Etna	795	1122	1135	–	–	1185	−0.002	0.024	0.068 (75.56 %)	0.062	0.028	0.090
Kīlauea (inner)	896	1069	1139	–	–	1162	0.050	0.079	0.012 (8.15 %)	0.152	−0.011	0.141
Kīlauea (outer)	891	–	1119	–	–	1159	0.054	0.063	0.042 (26.42 %)	0.151	0.008	0.159
Krafla	829	1010	1099	1122	1136	1154	0.088	0.046	0.065 (32.83 %)	0.137	0.061	0.198
La Palma	803	–	1096	–	–	1135	−0.007	0.060	0.093 (63.70 %)	0.085	0.061	0.146
Mauna Kea (exposed)	–	–	1052	1172	–	1205	0.546	0.275	0.044 (5.09 %)	0.830	0.034	0.864
Processed analogue material												
Green glass (air)	786	848	1171	1282	–	>1300	−0.007	−0.014	0.123 (120.59 %)	−0.017	0.119	0.102
Orange glass (reduced)	723	812	1131	1201	–	1221	−0.007	−0.020	−0.021 (43.75 %)	−0.034	−0.014	−0.048
Mauna Kea (reduced)	–	–	1033	1122	–	1171	0.151	0.088	0.074 (23.64 %)	0.253	0.060	0.313

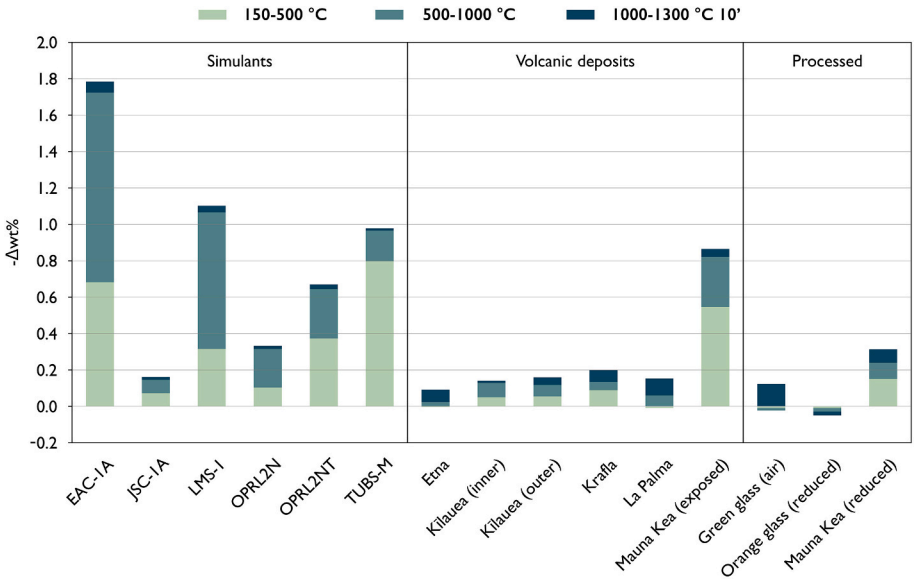

Fig. 2. Summarised cumulative mass loss over sample temperature ranges defined in Table 1.

secondary CO_2 peak. O_2 deviation is visually negligible. T_{AS} is nearly 90 °C above the next closest simulant, giving a melt interval of only 36 °C, with consequently little associated degassing above its solidus (0.001 wt %).

3.1.2. *Volcanic deposits*

The volcanic samples (Fig. 4), with exception of the non-fresh Hawaii ash, undergo comparable or weaker de-volatilisation to the simulant exhibiting least mass loss (JSC-1A). Etna ash displays a double CO_2 peak below 500 °C, which then tapers until about 700 °C. The effect on weight loss is marginal. H_2O release coincides with the larger of these two peaks between 400 and 500 °C, although oxidation offsets the mass loss resulting in slight net *gain* up to 500 °C (+0.002 wt%). Mass loss only perceptibly commences above 900 °C from H_2O and SO_2, and persists throughout the isothermal segment. The cumulative value of 0.090 wt% is the lowest of any natural sample considered. In stark contrast to the simulants, 76 % of Etna's weight loss occurs above 1000 °C; the absolute wt% in this range (0.068) is also larger than for any simulant. Major crystallisation occurs at 795 °C, with a second minor event at 1122 °C, just prior to T_{AS} at 1135 °C. There is no discernible second melting event before T_{AL} at 1185 °C, which lies within the range of simulants without an anorthosite constituent.

Crushed inner reticulite from Kīlauea features a relatively high first T_C at 896 °C, and a second at 1069 °C. Like Etna, water loss is consistently extremely small, though persists throughout the entire run, including at 1300 °C. Evolved CO_2 is the lowest of any fresh sample. Two isolated SO_2 releases around 500 and 1100 °C are observed. The melt interval is condensed over 23 °C, in which overlapping melt peaks are present. From 1300 °C CO_2 is consumed by the sample, contributing to an upturn in the cumulative mass loss curve; however, the net loss above 1000 °C remains positive.

The outer portion of the reticulite is slightly more volatile-enriched. The CO_2 signal is higher throughout, with a main degassing plateau between ~375 °C (coinciding with stronger oxidation) and 875 °C, and an additional small H_2O release between 1000 and 1100 °C. A marginally wider melt interval has only one clear melting event. Like the inner sample, mass gain is seen at the end of the isothermal segment. The capacity for the barely perceptible O_2 baseline deviation to account for this increase is more clearly demonstrated with the orange glass. However, an assessment of oxidation trends at these low concentrations is complicated by the aforementioned background impurity.

Krafla ash has a markedly higher SO_2 contribution before the onset of melting. Its melt interval is more staggered: three distinct events are observed during this 55 °C period. Like the outer reticulite, an early CO_2 peak under 500 °C is accompanied by more pronounced oxidation. Of the fresh samples, Krafla has the greatest water release in this first interval; more so than JSC-1A.

La Palma ash exhibits even greater weight gain than Etna below 500 °C (+0.007 %), attributed to oxygen uptake coinciding with very low initial H_2O. Evolved CO_2 remains small. SO_2 is a prominent contributor to mass loss, such that the sample has the highest absolute fractional mass loss (0.093 wt%) above 1000 °C of all the unprocessed material. Unlike Krafla, the major release is delayed until after T_{AL}. Common to the fresh deposits, the melting interval is on the order of only 40 °C.

Exposed Mauna Kea ash has a tapering H_2O trace from 200 °C until T_{AS}, and a broad CO_2 profile that extends to ~1150 °C. Oxygen is more heavily consumed from 250 °C until liquidus, peaking around 370 °C. Total mass loss is nonetheless comparatively high at 0.546 wt% up to 500 °C. SO_2 is released continuously from 500 °C in minor quantities, with a barely detectible contribution to mass loss at 1300 °C, alongside CO_2. No crystallisation is observed. An additional subtle endotherm before T_{M2} is unlabelled, as quantifying an onset from the shallow amplitude would be overly subjective. T_{AL} is the highest of the six volcanic deposits, at 1205 °C.

3.1.3. *Processed analogue material*

Two distinct crystallisation troughs are visible in the green glass synthesised under air (Fig. 5), dominated by the second at 848 °C. Although CO_2 is released below 800 °C, net mass loss is not seen until 1200 °C, after the onset of melting, in which O_2 is uniquely detected. This oxygen profile directly correlates with the independently measured mass loss rate curve. Water loss is negligible throughout (a slight baseline deviation is likely fed by an impurity from the purging gas itself), though a tiny expulsion is associated with crystallisation at T_{C2}. Total mass loss stands at 0.102 %. By 1300 °C, melting appears incomplete.

Orange glass produced under reduced conditions meanwhile returns an overall net mass gain of 0.048 %, due to the steady slight oxidation of the sample from ~250 °C. The H_2O profile matches that of the green glass. This higher-Ti composition is less stable after glass transition and crystallises earlier at 812 °C. A weak CO_2 signal extends until 1200 °C; the upturn ~1170 °C could provide an additional source of oxygen to drive a potential exothermic peak superimposed on the larger melting event, or alternatively indicate a double melting event in quick succession. T_{AL} is reached within experimental range, by 1221 °C.

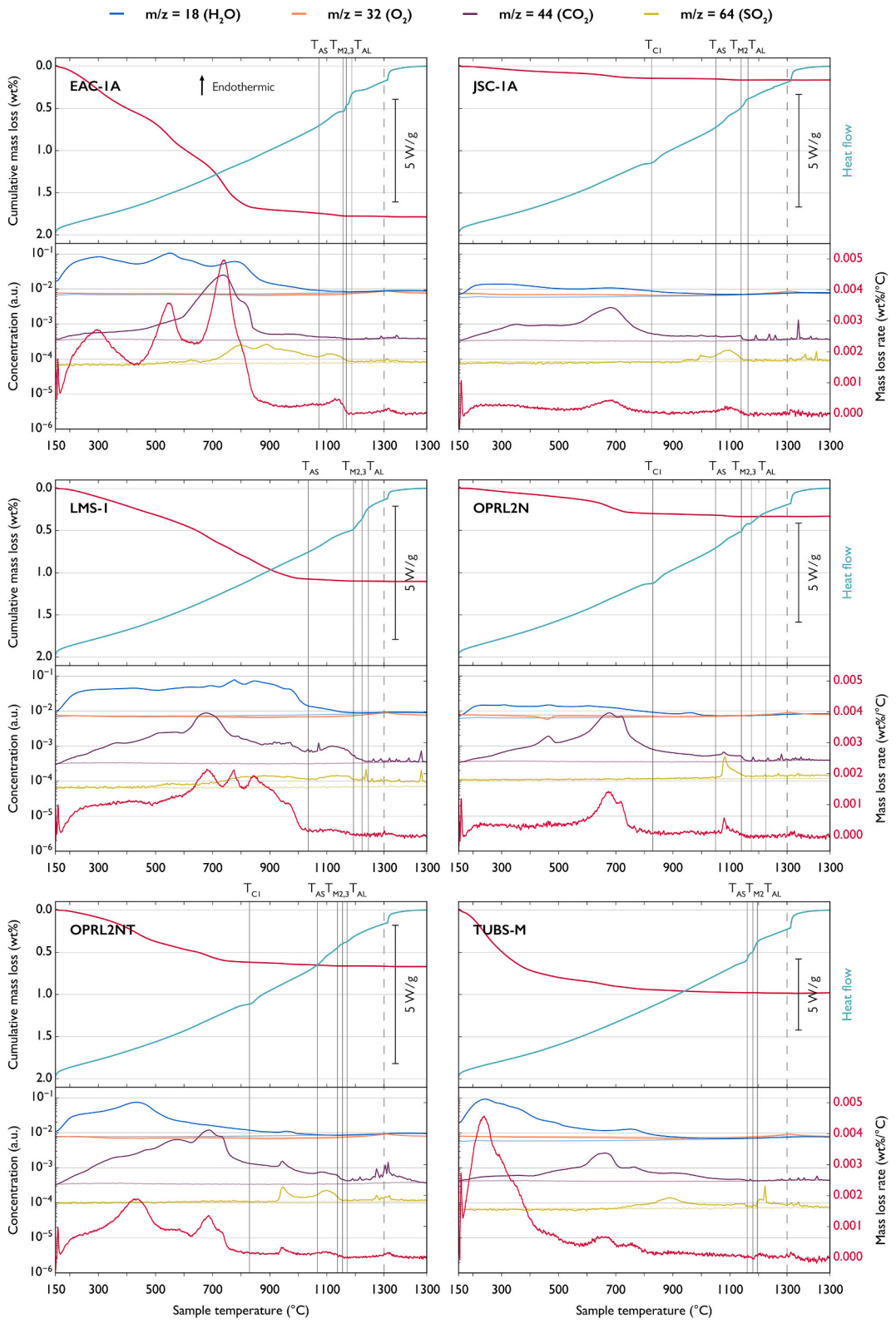

Fig. 3. Simultaneous DSC-TGA (upper subplot) and synchronous EGA (lower subplot) via mass spectroscopy performed on lunar mare simulants. TGA raw data is presented as cumulative mass loss normalised to the dried sample mass at 150 °C. DSC raw data is expressed as sample heat flow, with variable vertical scale. Mass loss rate is depicted on the lower plot for closer alignment with contributing gas species. EGA raw data collected as ion current is a proxy for relative gas concentration (arbitrary units) using the given mass-to-charge (m/z) ratios. The fainter curves are baselines for their corresponding colour. T_{Cx} and T_{Mx} represent characteristic temperatures associated with crystallisation peaks (if detectable) and onset of distinct melting events, respectively, whilst T_{AS} (= T_{M1}, i.e. first observable onset of melting) and T_{AL} are estimations of apparent solidus and liquidus temperatures as reported in Table 1. The subscript number 'x' denotes chronological occurrence.

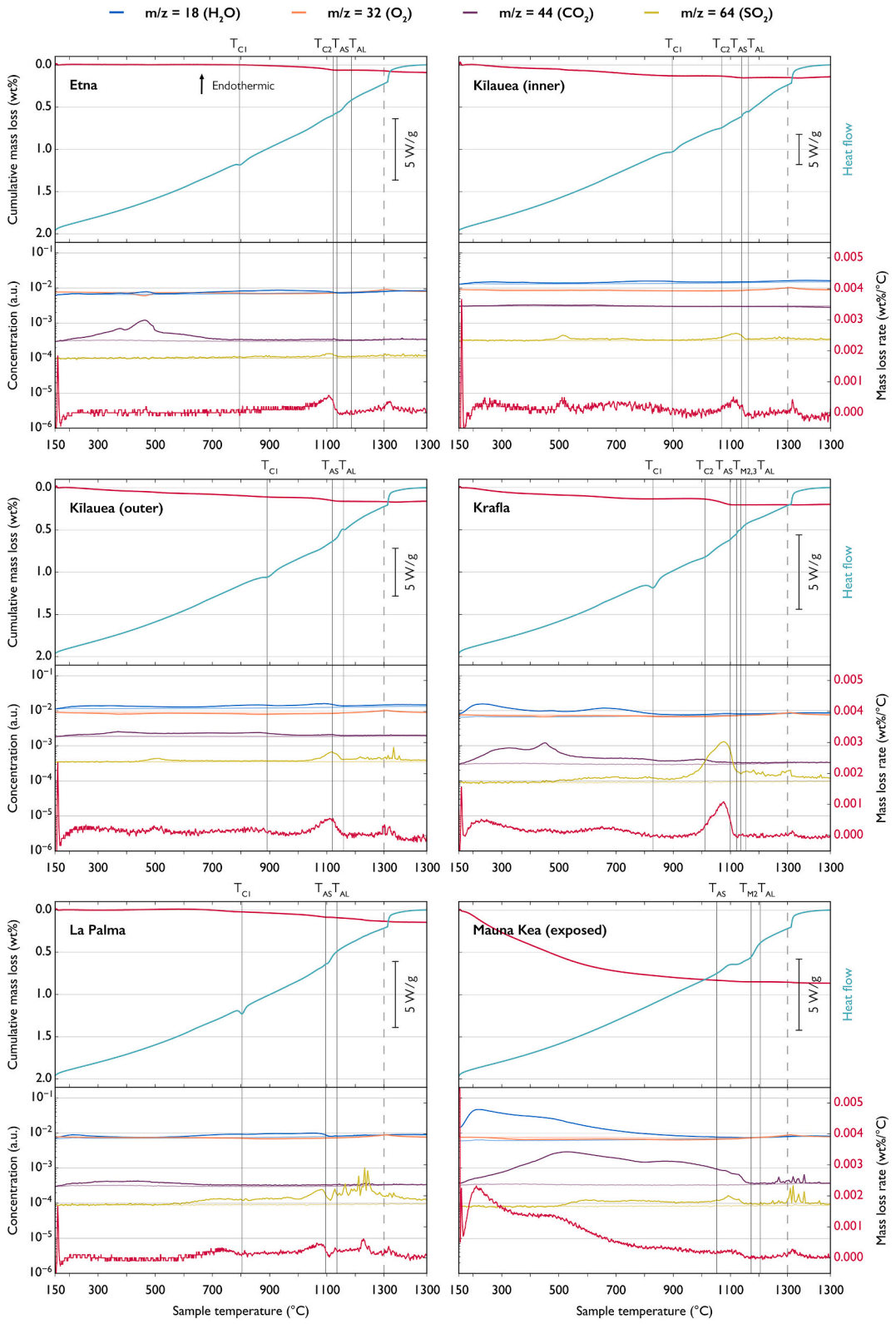

Fig. 4. Simultaneous DSC-TGA (upper subplot) and synchronous EGA (lower subplot) via mass spectroscopy performed on mostly fresh volcanic deposits. Labels are as described for Fig. 3.

Partial oxygen reduction of the Mauna Kea ash lowers overall mass loss almost three-fold, predictably coinciding with the sub-1000 °C interval. However, from 800 °C the CO_2 signature is comparatively elevated and increased oxidation is observed in association, peaking just after T_{AL} and steadily growing throughout the isothermal segment. The prior reduction procedure lowers the onset of melting by 19 °C and apparent liquidus by 50 °C.

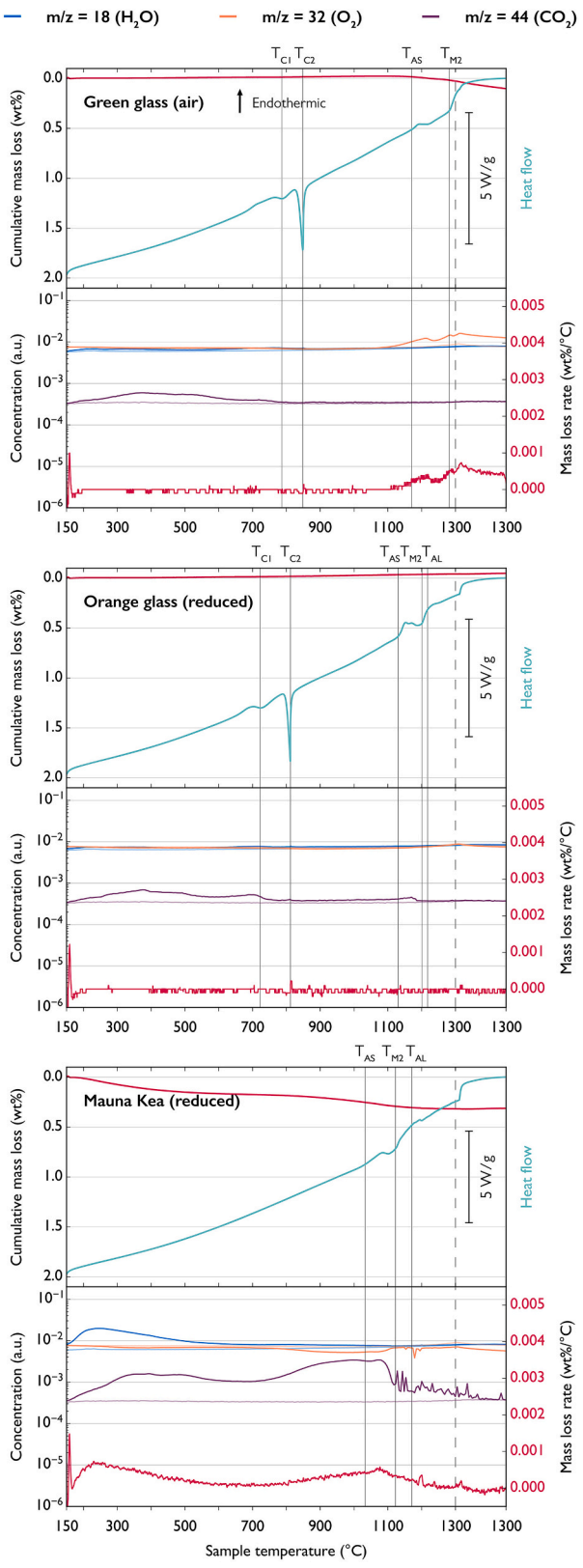

Fig. 5. Simultaneous DSC-TGA (upper subplot) and synchronous EGA (lower subplot) via mass spectroscopy performed on processed analogue material. Labels are as described for Fig. 3.

3.2. NPD

3.2.1. JSC-1A

Vertically stacked sequential diffraction patterns are shown in Fig. 6a. Phase identification is assisted by reported components (e.g. NASA, 2007) and the International Centre for Diffraction Data (ICDD)'s search indexing software SIeve+, drawing upon the Powder Diffraction File database PDF-5+. Scarcity of low angle reflections point to the absence of layered structures with large unit cells that incorporate water molecules (e.g. zeolites and phyllosilicates including clays). Accordingly, the general leftward slant of peak traces with temperature indicates thermal lattice expansion. The faint reflection at 1.30 $Å^{-1}$ (plausibly trace alunite, $KAl_3(SO_4)_2(OH)_6$) is the sole observation of subsolidus crystalline decomposition, becoming undetectable after around 325 °C as dehydration in Fig. 3 begins to taper. Branching reflections (e.g. 2.57 and 2.95 $Å^{-1}$) from around 300 °C are related to lattice distortion due to slight oxidation of Fe^{2+}, partially transforming ulvöspinel to ilmenite without detectable impact on the DSC profile. Drop off in intensity at 3.19 $Å^{-1}$ after 600 °C could be attributed to loss of the long-range magnetic contribution from magnetite above its Curie temperature. Peak strengthening approaching 800 °C is through crystallisation of the initial glass component. No evidence of any crystalline phase contributing to the elevated CO_2 signal around 600–750 °C is observed; given the cumulative mass loss of this reaction is less than 0.1 wt%, water-bearing phases encompassed, the associated mineral breakdown is unsurprisingly below neutron detection limit (~1 wt%). The recognition of alunite, though in proportions beyond general detection, is possible with these counting statistics only through enhanced H sensitivity. Melt onset is first observed in the strongest plagioclase (bytownite) reflection centred on 1.96 $Å^{-1}$, as well as the prominent pyroxene (augite/diopside) peak at 2.08 $Å^{-1}$ during the count ending 1011 °C (inset i). The progressive decrease in crystalline intensity is accompanied by a subtle rise in the broad, diffusely scattered baseline, indicating loss of long-range order and the development of an amorphous component. Having adjusted for the systematic underestimation of the thermocouple, the onset of melting is lower than the DSC-derived value by ca. 40 °C.

3.2.2. TUBS-M

The release of adsorbed and interstitial water largely below 400 °C is marked by a broad decrease in the diffuse baseline intensity (Fig. 6b). Subsequently, two distinct structural decompositions are identified (inset ii and iii). In the count ending 628 °C through to 779 °C, dehydrated chabazite ($(Ca,Na)Al_2Si_4O_{12}·6H_2O$) is a candidate for the decaying low-angle peak at 0.68 $Å^{-1}$, with an additional zeolite, analcime ($NaAlSi_2O_6·H_2O$), at 1.13 $Å^{-1}$ from 761 °C until loss of detection at 942 °C. Contrary to the generally observed lattice expansion, partial collapse of structural voids following zeolitic water loss leads to a reduction in unit cell volume. This contraction is more pronounced for analcime owing to constrained water positions and a rigid framework that cannot compensate as flexibly. With relatively open channels, chabazite releases water more readily. No potential carbonate phases nor sulfur-bearing candidates are observed within detection limits. Melt onset is detected as early as 981 °C, again first in the 1.96 $Å^{-1}$ plagioclase peak (inset iv), well below the 1161 °C predicted by DSC (reproducible to ± 5 °C).

Suspecting that the increased water content of TUBS-M relative to JSC-1A is responsible for the more pronounced solidus reduction, the protocol was repeated with TUBS-M dehydrated at 500 °C in air for 24 h prior. Fig. 7a illustrates the differences at select temperature increments. Under ambient conditions, the diffuse water contribution is evident from the vertical separation of the two curves. Peaks at 0.68 and 1.45 $Å^{-1}$ (chabazite) are barely visible in the partially dehydrated sample – prolonged exposure at 500 °C is sufficient to approach thermodynamic equilibrium, contrasted with inset ii in Fig. 6. The statistics of the repeat pattern appear weaker, although the trace is entirely reproducible. At

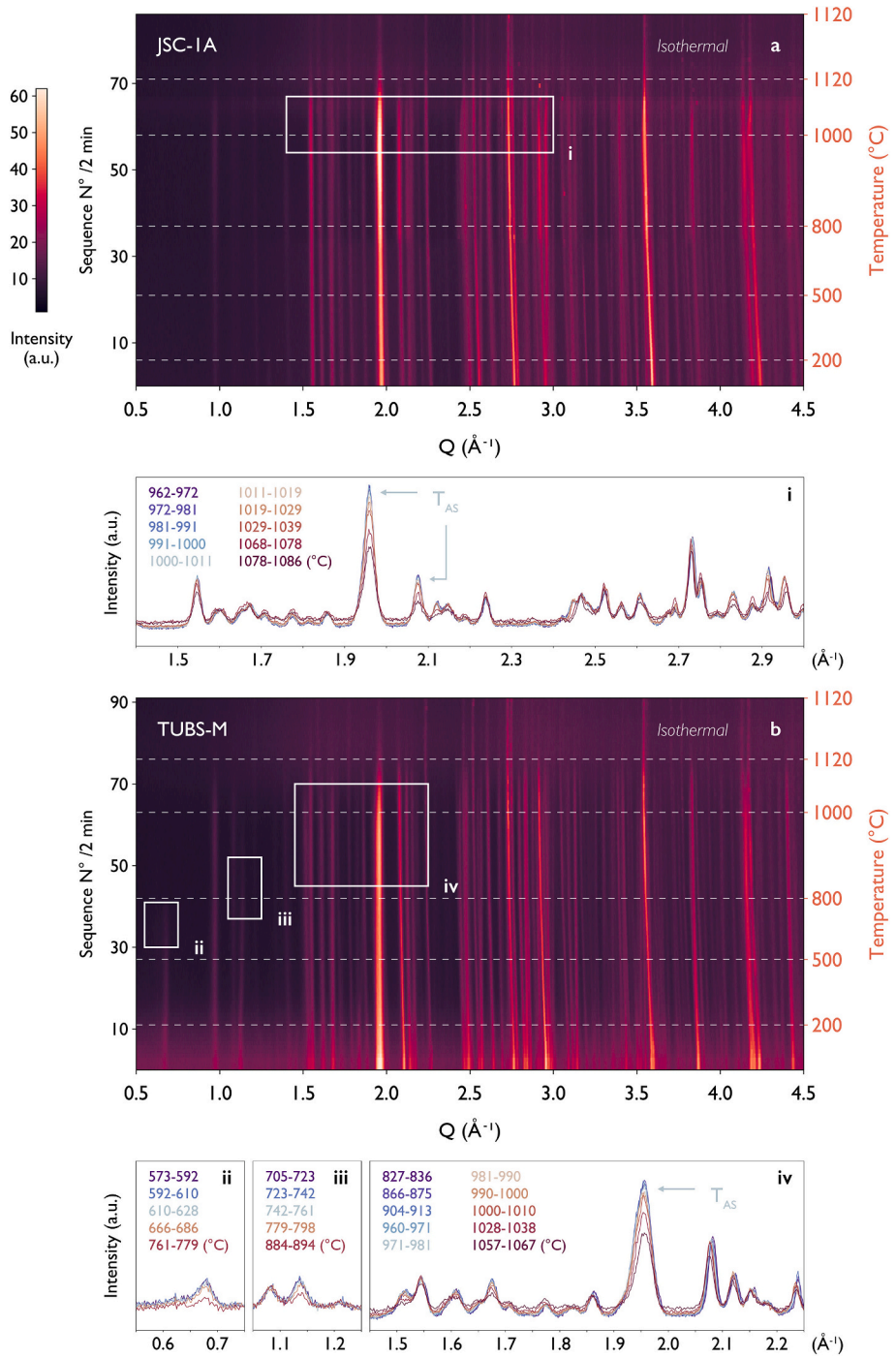

Fig. 6. In situ NPD of (a) JSC-1A and (b) TUBS-M collected at D20 (ILL). Successive patterns integrated over two-minute intervals with continuous temperature ramping (10 °C/min < 820 °C; 5 °C/min 820–1120 °C) are vertically stacked. Crystalline decomposition and melt onset (T_{AS}) are highlighted in inset i-iv; not all temperature intervals contained in the outlined range are displayed and vertical scale varies between plots.

1000 °C both samples are totally dehydrated and raw TUBS-M has just begun to melt. As the incoherent baseline contributions converge, no significant difference in hydrogen content remains between the two, i.e. excess trapped intergranular water vapour is not discernibly present in the raw sample. There is a marked increase in melt extent in the raw sample by 1100 °C that therefore cannot be explained by ongoing water presence. However, after holding for a further 30 min the pre-treated sample is largely able to catch up. When melting is kinetically constrained, even beyond the water evacuation range, the dehydration history appears to influence melt onset and development. Furthermore, with a residual 0.169 wt% loss between 500 and 1000 °C (more than double JSC-1A), the apparent solidus of the partially-dehydrated sample (1015 °C) remains almost 150 °C below the DSC-determined onset. To indicate potential differences in the progression of partial melting, Fig. 8 additionally compares the temperatures at which the first-melting plagioclase reflection surpasses 80 % and 70 % of its maximum intensity. The temperature discrepancy between samples in both cases is consistent at ca. 42 °C, marginally higher than for T_{AS} (34 °C).

This picture is complicated when increasing the starting amorphous fraction by 30 wt% through incorporation of soda-lime glass to promote earlier melting (Fig. 7b). Absolute peak intensities at ambient temperature are diminished by ~30 % as expected. Both samples undergo

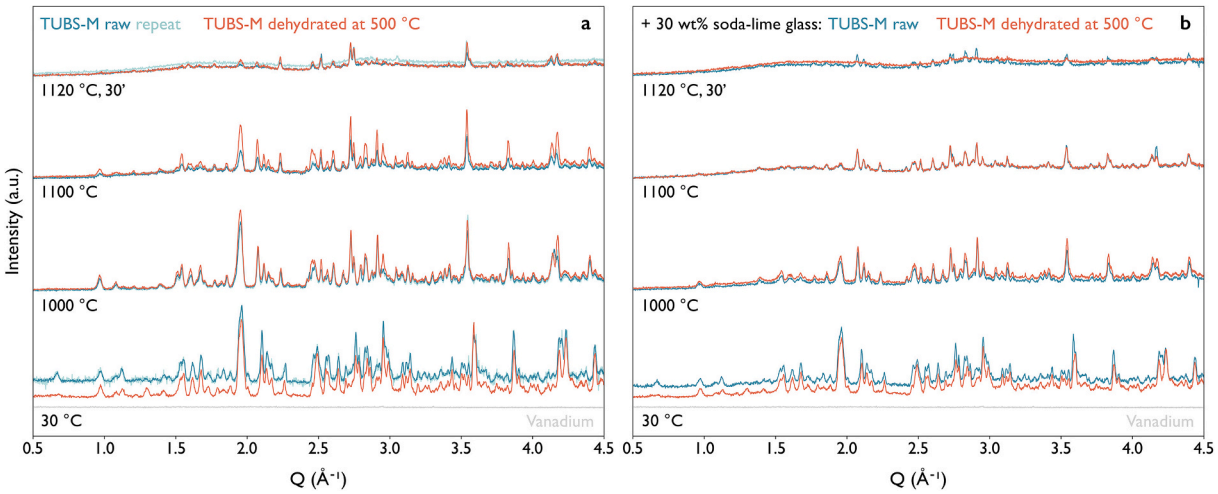

Fig. 7. Select in situ NPD patterns contrasting the evolution of as-received (raw) simulant and after pre-treatment at 500 °C in air for 24 h. (a) Fully crystalline starting samples. (b) Additionally incorporating 30 wt% soda-lime glass (45–90 μm bead size), following any pre-treatment.

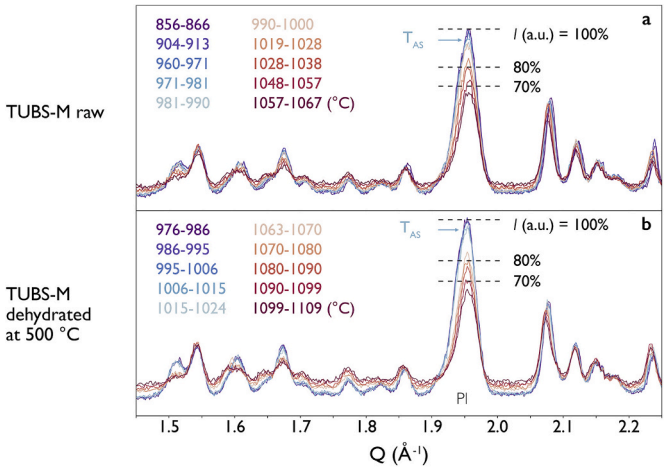

Fig. 8. In situ NPD of (a) TUBS-M and (b) TUBS-M pre-dehydrated at 500 °C in air for 24 h. Dashed lines highlight melting onset and progression (exceeding 80 % and 70 % maximum intensity) in the first-melting peak at 1.96 $Å^{-1}$ (plagioclase).

increased though comparable melting through 1000 and 1100 °C. Unlike the initial fully crystalline samples, patterns diverge after holding at 1120 °C; the raw sample evolves little over the 30-min increment, whereas the partially dehydrated version is nearly completely molten. Thus, the addition of soda-lime glass beads appears to preferentially encourage melting of the partially dehydrated crystalline component, whereas the raw pattern remains relatively unchanged in melt extent at 1120 °C aside from the proportional reduction in crystalline intensity.

4. Discussion

4.1. Sample trends

Simulants exhibit higher mass loss and volatile release at sub-solidus temperatures than fresh volcanic materials and synthesised glasses, though overlap exists between JSC-1A and unexposed ash. Among the simulants, over an order of magnitude difference in cumulative mass loss is seen (Fig. 2) in both 150–500 °C (between JSC-1A and TUBS-M) and 500–1000 °C (between JSC-1A and EAC-1A/LMS-1) ranges. Conversely, they exhibit comparable or in many cases slightly lower mass loss from 1000 to 1300 °C than the fresh material. For all 15 samples, degassing persists from room temperature until at least the apparent liquidus, although mass loss is not perceptible throughout.

The relative magnitude of species contributions is largely consistent among simulants, however, the loss rate is not always dominated by water (notably with material from the San Francisco Volcano Field). This distribution is more in line with the fresh samples, whose water contribution is small – or negligible in the case of Etna and La Palma ash. For these five rapidly collected deposits, mass loss rate is shaped by SO_2. The profile for synthesised glasses is driven by uptake or release of oxygen, depending on the fugacity (fO_2) during formation.

4.2. Mass loss origins

Here we combine insights from STA and NPD to briefly attribute mass loss in the samples. Sequential detection of H_2O, CO_2, and SO_2 is geologically consistent with dehydration, decarbonation, and desulfation (in their several forms) during decomposition reactions, diffusion from volcanic glass, exsolution from the melt phase, as well as the removal of fluid and melt inclusions. Below ~300 °C, adsorbed, interlayer, and caged water is liberated from secondary minerals, while crystalline (·H_2O) water may persist to ~600 °C depending on the mineral phase. These develop in low-temperature environments through processes associated with weathering (e.g. clays), hydrothermal activity (e.g. zeolites), diagenesis (e.g. caliche), or direct precipitation from aqueous solutions (e.g. gypsum, hydromagnesite). Water evolution is sustained to 900 °C from the breakdown of more tightly-bound hydroxyl groups (e.g. amphiboles, micas). Early release of carbon-containing species is found in all cases except Kīlauea (inner) from adsorbed CO_2 or organic residues. Common carbonate weathering products can dissociate into metal oxides and CO_2 from ~400–900 °C. Low temperature isolated SO_2 detection (e.g. around 500 °C in the Kīlauean reticulites) may be ascribed to fluid inclusions, which can be released over a broad temperature range, depending on the thermal stability of the host mineral. If volcanic glass is present, the majority of dissolved hydrogen, carbon, and sulfur species are released following the glass transition (typically 600–800 °C), as its structure relaxes and permits increased diffusion rates. Under inert atmosphere, SO_2 in the range ~ 550–750 °C is a by-product of two-step sulfide decomposition, primarily pyrite (FeS_2), provided oxygen is available from the surrounding phases or purging gas impurity (Hu et al., 2006). Non-lunar sulfates such as anhydrite ($CaSO_4$, the dehydrated form of gypsum) contribute to the signal up to ~1000 °C. The reduced sulfur species H_2S was here below detection limit.

Approaching solidus temperatures, the (re-)emergence of SO_2 loss in

all simulants (Fig. 3) and natural material (Fig. 4) can be attributed to either melt inclusions in primary crystals, or lattice-bound (structural or impurity) volatiles from softening and then partial melting. Stepwise heat flow indicates incongruent melting, particularly for simulants of more hybrid sources. Beyond the liquidus, punctuated signals from SO_2 and CO_2 containing-bubbles are indicative of low viscosity melt (on the order of $10^{1.12}$ Pa·s, TUBS-M at 1300 °C (Stapperfend et al., 2024)). Their reception is not instantaneous (e.g. a lag in the material of Hawaiian origin), suggesting some time is required to allow volatile products to reach the melt surface for a given temperature. Exsolution of residual water is also observed therein (both reticulites), as its solubility in the complete melt steadily decreases. Where the gas traces of SO_2 and CO_2 align, for example between 900 and 1150 °C in OPRL2NT, the decomposition reactions of sulfates can be carbon-assisted, as highlighted by Petkov and Voecks (2023). While the major degassing period for simulants ends between 700 and 1000 °C (Fig. 3), for Etna and La Palma samples devolatisation comparatively accelerates above 1000 °C, as these volatile sources dominate (Fig. 4).

Oxidation, when occurring, appears from 250 °C onwards. The signal is particularly enhanced during an isolated CO_2 event around 460 °C with OPRL2N, Etna, and Krafla ash. Reactions involving transient oxygen and granular surfaces are typically Fe^{2+} to Fe^{3+}, as seen with the ulvöspinel unmixing in JSC-1A, but can apply to glass as well. Besides iron, oxidising reactions may involve carbon (i.e. combustion), sulfur (e.g. pyrite), titanium (e.g. titanomagnetite, $Fe^{2+}(Fe^{3+},Ti)_2O_4$), and chromium (e.g. chromite, $FeCr_2O_4$), all of which have been reported among the samples (e.g. Schrader et al., 2008). For strongly reduced samples (Kīlauea, Krafla, orange glass, and processed Mauna Kea) degassing has tapered to the extent that oxidation drives net mass gain above 1300 °C. In the absence of sufficient O_2, the molten inner reticulite also consumes CO_2.

4.3. Analogues in the lunar context

Direct measurements from Chang'e-5 (11–87 ppm H_2O/OH particle size-dependent average (Lin et al., 2022, 2024)) and revisited Apollo samples (Liu et al., 2012) constrain typical bulk mare soil to sub-100 ppm H_2O/OH, consistent with the background level from near-infrared spectra within ±35° latitude (Milliken and Li, 2017). Attributing the majority of mass loss under 1000 °C to water, simulants release two to three orders of magnitude (0.15–1.72 wt% from JSC-1A to EAC-1A) more, reduced by an order in the unexposed material (0.02–0.13 wt% from Etna to Krafla). This simplistic assumption discounts varying mass gain from oxygen uptake. Exceptions exist for areas of localised enhancement in various pyroclastic deposits and KREEP-rich material up to several hundred ppm water equivalent hydrogen; with a perspective towards attractive landing sites for ISRU, it is notable that the water mass of the Aristarchus Plateau pyroclastic deposit, for instance, has been calculated as a significant fraction of that estimated for the lunar poles (Lawrence et al., 2022). In contrast to the initial Apollo vacuum pyrolysis studies (Table S2), this study underestimates absolute volatile availability in the analogues as melting under atmospheric pressure prolongs solubility, particularly of water (Holtz et al., 1995).

Overlap in the carbon content range of volcanic melt from terrestrial and lunar sources is reported. Measured abundance in lunar mare soils and regolith breccias has been found to reach 216 ppm C (average 109–154 ppm among Apollo mare locations, concentrated in the finest fractions: up to 500 ppm < 53 μm (Moore et al., 1970; Gibson, 1977; Haskin and Warren, 1991)), though more than half (51–98 %, $n = 6$ basalts) of which is likely to be associated with terrestrial contaminants below 600 °C (Mortimer et al., 2015). If speciated entirely as CO_2, this upper (contaminated) bulk value is equivalent to 792 ppm. However, CO is the primary exsolved C species on the Moon (Rutherford and Papale, 2009); across the realistic range of lunar fO_2, the degassed CO_2 proportion is estimated between 4 and 29 % (Varnam et al., 2024). Water-poor subaerial ocean island basalts (OIB) like Kīlauea typically retain up to 350 ppm CO_2 (95 ppm C, excluding CO contribution) in quenched glass, though highly degassed products in low-viscosity systems characteristic of OIB may contain as little as <10 ppm CO_2 (Anderson and Brown, 1993; Johnson et al., 1994). Under standard oxidising conditions during eruption, most carbon in the system preferentially exists as CO_2 (Ni and Keppler, 2013), which remains more soluble than CO at high temperature by integrating into the melt via carbonate complexes. Supposing equal C abundance, these diverging redox and solubility behaviours differentiate lunar and terrestrial degassing profiles. Furthermore, whereas CO readily diffuses to escape from silicate melts, lower-mobility CO_2 tends to accumulate (Koch and Schmidt, 2023) until saturation is reached, so that larger gas voids may be expected.

Sulfur is locally more heterogeneous than hydrogen or carbon on the Moon. It is comparable or even enriched in lunar basalts relative to their terrestrial counterpart (up to 0.30 wt% versus less than 0.15 wt% (Taylor et al., 1991)), with 440–1400 ppm S (mission-dependent average 748–1280 ppm) identified in mare or mixed terrain Apollo soil (Gibson, 1977), primarily as troilite (FeS). In Earth-based basaltic melts, the two dominant forms are sulfide (S^{2-})- and sulfate (SO_4^{2-}). Their ratio is strongly dependent on fO_2 over an interval (Δnickel-nickel oxide (NNO) buffer = −0.8 to +1.2, Wallace and Carmichael, 1992) encompassing redox conditions of potential analogue sources, where preferred sulfur speciation will vary accordingly. Whilst mare simulants tend to be derived from intraplate continental settings, fresher samples additionally include more oxidised environments i.e. OIBs (e.g. La Palma, Burton et al., 2023) and subduction-influenced intraplate basalts (e.g. Etna, Metrich and Clocchiatti, 1996). Sulfides are typically less thermally stable and degas at lower temperatures than sulfates (Gazulla et al., 2009) although oxygen fugacity influences the precise release pathways. Under lunar fO_2, sulfur only occurs in its reduced state. When saturation is reached, reduced species including S_2, H_2S, COS, and CS_2 (ten Kate et al., 2010; Varnam et al., 2024) tend to escape more readily owing to their higher diffusivities, likely leading to more efficient release than in sulfate-rich melts. Outside of the volatiles considered in this study, N, F, and Cl species are additionally present in lunar soils up to a few hundred ppm (McCubbin et al., 2015).

The observed release patterns herein are broadly consistent (Fig. 9) with previous analyses on (to some extent contaminated) regolith (Gibson and Johnson, 1971; ten Kate et al., 2010; Mortimer et al., 2015; Verchovsky et al., 2020a), even if the origin and concentrations of volatiles diverges. Sustained H_2 or water release is derived from solar wind implantation, impactors, or indigenous OH in trace minerals like apatite, with a similar drop off around solidus. Agglutinitic and impact glasses, rather than minerals, have been shown to host the majority of H (Liu et al., 2012; Zhou et al., 2024). At latitudes below 30° (where surface temperatures exceed 400 K), the water content correlation with optical maturity diminishes (Li and Milliken, 2017). The integrated water abundance in Apollo soil 12070 (Table 2) is inflated above known values as the gas transfer was not optimised for water analysis. Below 600 °C, the carbon contribution is dominated by terrestrial sources. Sulfur is absent below 1000 °C. Exponential growth of carbon and sulfur species above ca. 1000 °C highlights a consistent degassing between simulants, fresh material, and original regolith: that of endogenous gases dissolved in the magma. Later-stage vesiculation arising from $S_xO_y/CO_x/N_2/H_2S$ exsolution therefore is also to be expected during processing of lunar regolith, a conclusion similarly drawn by Wilkerson et al. (2023). To our knowledge, there is no recorded lunar benchmark specifically for post-solidus volatile abundances in bulk regolith. Sulfur and carbon released above 1000 °C mainly originates from troilite (magmatic, or a product of vapour or fluid interaction)/carbide decomposition, volcanic glass, or redistributed sulfur/trapped exogenic organic material in vapour-condensed impact glass coatings or in mineral defects (McCubbin et al., 2015).

Although it is the most abundant volatile in lunar soils and volcanic glasses (Gibson, 1977; Saal et al., 2008), studies of lunar S have been

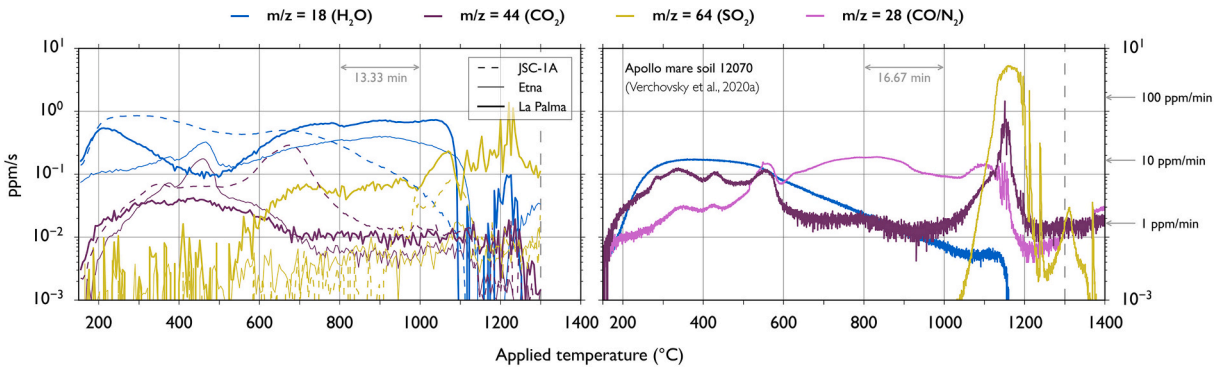

Fig. 9. Rate of release profiles for H_2O, CO_2, and SO_2 of select analogues (left) and Apollo mare soil 12070 (right). MS of the lunar sample (Verchovsky et al., 2020a; A. Verchovsky, personal communication, March 2025) was performed under a baseline pressure of 10^{-3} mbar according to the setup in Verchovsky et al. (2020b). An additional reference curve at $m/z = 28$ is therefore included; CO expectedly dominates this signal with a small contribution from N_2. Linear heating rates over the range are 15 °C/min for the analogues, and 12 °C/min for the Apollo sample. The release rate (ppm/s) is normalised to values in Table 2: for H_2O and CO_2 total ppm corresponds to that stated for 150–1300 °C, whereas SO_2 uses the elevated estimation from T_{AS}-1300 °C.

limited compared to H, C, and N. Previous work indicates positive correlation of sulfur with TiO_2 concentration, and negatively with Al_2O_3, in multiple sample types, including soils (e.g. Gibson et al., 1977; as compiled in Renggli et al., 2024). A positive correlation between sulfur content and $\delta^{34}S$ exists convincingly in pyroclastic glasses, derived from magmatic processes and variations in source composition (Saal and Hauri, 2021). In lunar soils, a similar correlation is only loosely observed within individual source missions, linked with increasing maturity (Renggli et al., 2024). In contrast, impact glasses returned by Chang'e 5 show decreasing S abundance with increasing $\delta^{34}S$ (Wang et al., 2024), attributed to isotropic fractionation during impact degassing, some of which may then condense on regolith grains (Dottin et al., 2022). Sulfur-rich material is preferentially concentrated in the fine grain, though with a tendency for S concentration to initially fall, before rising with decreasing grain size (Rees and Thode, 1974). Integrated SO_2 abundance in soil 12070 exceeds the approximated concentrations in the La Palma ash sample and JSC-1A by one to two orders of magnitude, respectively. The difference in total S budget is significantly underestimated without the unmeasured reduced contribution (e.g., as presented in ten Kate et al., 2010). Terrestrial analogues are then more likely to resemble the post-solidus volatile budgets of lunar material sourced from lower-Ti, more felsic compositions, which, if targeted, would limit bubbling after melt onset. As temperatures exceed 1200 °C in vacuum, degassing in both terrestrial and lunar volcanic material will encompass vaporisation of the constituent materials, fundamentally altering the composition of the remaining melt (Šeško et al., 2024).

Fresh volcanic material bridges the magnitude and distribution of documented mass loss in lunar soils, with as little as a few hundred ppm of water. 76 % of the total 0.090 wt% loss between 150 and 1300 °C in Etna ash is above 1000 °C, compared with ca. 91 % in the 1000–1400 °C range for Apollo 11 and 12 soils (Gibson and Johnson, 1971). These fresh samples are highly glassy which is not only relatively more stable against chemical weathering (not applicable here due to rapid collection), but may initiate volatile release more readily above the glass transition temperature through enhanced mobility in the supercooled liquid state. By contrast, flash heating preferentially sequesters volatiles in quenched lunar impact melt (Liu et al., 2012). The high glass content and arid origin of JSC-1A source material is a strong determiner of its low mass loss, although minor substitution of basalt with anorthosite can dramatically raise this, i.e. 10 wt% in OPRL2N doubles mass loss below the solidus. Increasing volcanic glass fraction is not a realistic prospect; while lunar pyroclastic glasses have local pockets of abundance, these are a minor (typically <5 vol% (McKay et al., 1991)) component of mare regolith. Elevated analogue glass content is not problematic per se as a sintering agent in processing applications, however, as largely unimitated impact glass (ca. 3–5 vol%), glass-containing agglutinates (5–65 vol%, average 25–30 vol%), ropy glasses, and shocked minerals (maskelynite) cumulatively make up a comparable fraction of the lunar soil (McKay et al., 1991). Although JSC-1A exceeds the Etna ash water content almost twofold, its more tapered release above 800 °C (Fig. 9) is potentially less influential for melt onset, provided the earlier evolved gases can be evacuated. The H_2O degassing rate nonetheless remains an order of magnitude higher than soil 12070 around T_{AS} (1051 °C).

4.4. Significance of volatiles for sintering and melting applications

We refer to approximations of the solidus and liquidus for specific conditions of pressure, rate, and fO_2, but they are not thermodynamically-determined temperatures, which would neither be applicable to ultimate lunar processing conditions. Partial and total gas pressures influence both reaction kinetics and the efficiency of volatile degassing itself (Zhang and Ni, 2010). Water vapour is known to enhance catalytic decomposition of carbonates (Giammaria and Lefferts, 2019) and sulfates (Gallagher et al., 1970). By way of example, caliche, a multi-constituent sediment primarily composed of calcium carbonate, has been proposed as the main CO_2 source in JSC-1A (Street Jr. et al., 2010). Its CO_2 trace peaks earlier than for isolated calcium carbonate decomposition, demonstrating the effectiveness of water (captured in the caliche matrix and alunite) to aid the breakdown of the $CaCO_3$ structure via formation of intermediate species (e.g. $Ca(HCO_3)_2$) by over 100 °C. Even though water is no longer detectable by 1000 °C in Fig. 7a, prior water loss appears to have facilitated earlier melting of the raw TUBS-M sample. Hydration-weakening of grain boundaries, e.g. via water-mediated diffusion or by enhancing reactivity, can lower the activation barrier to incipient melting, potentially initiating the first reduction in crystalline coherence. Once underway, the rate of intensity decrease initially appears consistent (Fig. 8), suggesting that the melting process itself is proceeding at a similar kinetic pace. Prolonged heating at 1120 °C (Fig. 7a) allows the samples to approach equal melt fractions once water-related kinetic advantages are no longer decisive and residual resistances (e.g. structural rigidity, dry grain boundaries) are overcome. The much larger partial pressure within TUBS-M compared to JSC-1A overwhelms the contribution towards lowering solidus from a 10^7-fold reduction in external atmospheric pressure (recognising trapped inter-granular air during capillary loading will locally reduce this figure), at moderately slower heating. A pressure gradient is expected towards the container opening due to gas migration (Figs. 10 and S2). In more hydrated systems, rapid degassing can steepen chemical potential gradients. If gases cannot escape efficiently, pressure builds up, and the resulting increase in volatile solubility subsequently suppresses further bulk degassing. In contrast, drier samples exhibit steadier degassing and

Table 2
Integrated concentrations of H_2O, CO_2, and SO_2 in Apollo mare soil 12070 and select analogues. Apollo data are derived from Verchovsky et al., 2020a. In parenthesis are the contributions of CO_2 and SO_2 towards the overall C and S budgets. Ranges refer to applied (furnace) temperature, except T_{AS}, which pertains specifically to sample temperature, consistent with values in Table 1. Integrated ppm is calculated by normalising the sum of the relative gas fractions (H_2O, CO_2, SO_2, and O_2) against the absolute measured mass loss fraction. For asterisked values, oxygen is neglected in the calculation as apparatus diffusion significantly contributes to the total. The increase in SO_2 and to a lesser extent CO_2 ppm over narrower intervals is a consequence of the calculation a) assuming all gases behave similarly across the full range, and b) normalising a greater relative share of gas concentration over a considerably smaller denominator at high temperature in water-dominated systems.

	Integrated ppm											
	Apollo mare soil 12070 (Verchovsky et al., 2020a)		JSC-1A simulant			Etna volcanic ash			La Palma volcanic ash			
	150–1400 °C	1000–1300 °C	150–1300 °C	1000–1300 °C *	T_{AS}-1300 °C *	150–1300 °C	1000–1300 °C *	T_{AS}-1300 °C *	150–1300 °C	1000–1300 °C *	T_{AS}-1300 °C *
$m/z = 18$, H_2O	316 (0.03 wt%)	4	1564 (0.16 wt%)	47	2	906 (0.09 wt%)	474	78	1598 (0.16 wt%)	597	94
$m/z = 44$, CO_2 (C)	324 (89)	124 (34)	244 (67)	59 (16)	67 (18)	111 (30)	18 (5)	12 (3)	80 (22)	28 (8)	49 (13)
$m/z = 64$, SO_2 (S)	1533 (766)	1529 (765)	5 (3)	29 (15)	36 (18)	7 (4)	15 (8)	19 (10)	88 (44)	165 (83)	354 (177)

maintain lower internal pressures, potentially enabling more efficient volatile escape.

Above the solidus, any dissolved water retained in the melt helps depolymerise the silicate network and enhance cation mobility, as well as accelerating diffusion of CO_2 (Koch and Schmidt, 2023). The effective reduction in viscosity of the melt phase encourages bubble migration and expansion, which are in turn pathways for further degassing. However, water-rich melts can dissolve and retain greater amounts of other volatiles before exsolution begins (Mysen, 1976). Formation of gas bubbles can also temporarily raise the effective local viscosity as the melt must deform around many small inclusions. Relatively wet melts, e.g. late release simulants like LMS-1 or EAC-1A, or Kīlauea, may then follow less predictable viscosity evolution during melting due to the fluxing effect of volatiles destabilising the Si-O-Si framework. Meanwhile, drier systems depend on more gradual temperature-driven depolymerisation, with implications for material workability. Faster heating leads to oversaturation and rapid bubble nucleation and growth (e.g. Lim et al., 2023), as well as considerable broadening of evolved gas peaks (ten Kate et al., 2010), whereas slower rates permit steady-state conditions to be approached. Although the hydrogen and amorphous contents of both raw and pre-dehydrated TUBS-M converge upon holding at 1120 °C (Fig. 7a), the diverging textures in Fig. 10 indicate that degassing history still influences crystallisation kinetics. The raw sample sustained greater volatile loss during the heating programme, possibly creating chemical and structural heterogeneities that acted as nucleation triggers during cooling. These effects were most pronounced near the capillary edge, leading to the observed microcrystalline textures. In contrast, the pre-treated sample had already lost most of its water and reached structural equilibrium prior to high-temperature treatment, resulting in a more uniform melt structure and correspondingly homogenous texture on cooling. Further ex situ investigation (e.g. via SEM-EDS/EBSD or Raman) could offer more detailed insights into these cooling textures.

The mechanism by which vacuum conditions induce greater mass loss has been explained in terms of extended sulfur outgassing towards maximum temperatures due to earlier melt onset (Wilkerson et al., 2023), and more effective outward gas transfer (Lim et al., 2023) from heightened chemical potential gradient between the melt and its surroundings, thereby increasing diffusive flux. Even under so-called vacuum, an inevitable gradient of volatile vapour will locally emerge. These volatile by-products can transiently convect, aiding the heat transfer mechanism for furnace sintering and melting more significantly than for laser irradiation, where such contributions are proportionally less impactful under higher imposed temperatures. With complete melting, deviations in the target temperature are more forgiving. It remains to be determined at what level nominal vacuum becomes material-limited, and where negligible returns of effort are seen. Petkov and Voecks (2023) recommend no perceivable advantage beyond 10^{-6} mbar with JSC-1A, to which we suggest better than 10^{-4} mbar has diminished benefit for more heavily weathered untreated simulants like TUBS-M. Non-lunar oxidation is observed in a majority of cases from ca. 200 ppm apparatus contamination; although such levels would likely be absorbed into the already-saturated melt as part of the silicate network, higher concentrations (including via dissociation of volatiles) could affect liquidus temperatures if more refractory metal oxide crystals are stabilised under higher oxidation states. In an important distinction for volatile extraction efforts, O_2 release does not occur when the synthesised glass is formed under reducing conditions. We speculate this is not down to the difference in Ti content between the orange and green glasses. So far, no lunar-like analogues have been produced starting from oxides using a gas mixing furnace on account of practicality and volumes involved; gas release from samples produced under different redox states should be further studied, particularly in view of imitating accurate lunar C and S speciation. Simulating iron in the predominantly reduced state Fe^{2+} would better replicate its role as a network modifier in lunar melts, leading to lower viscosity (Dingwell, 1991; Di Genova

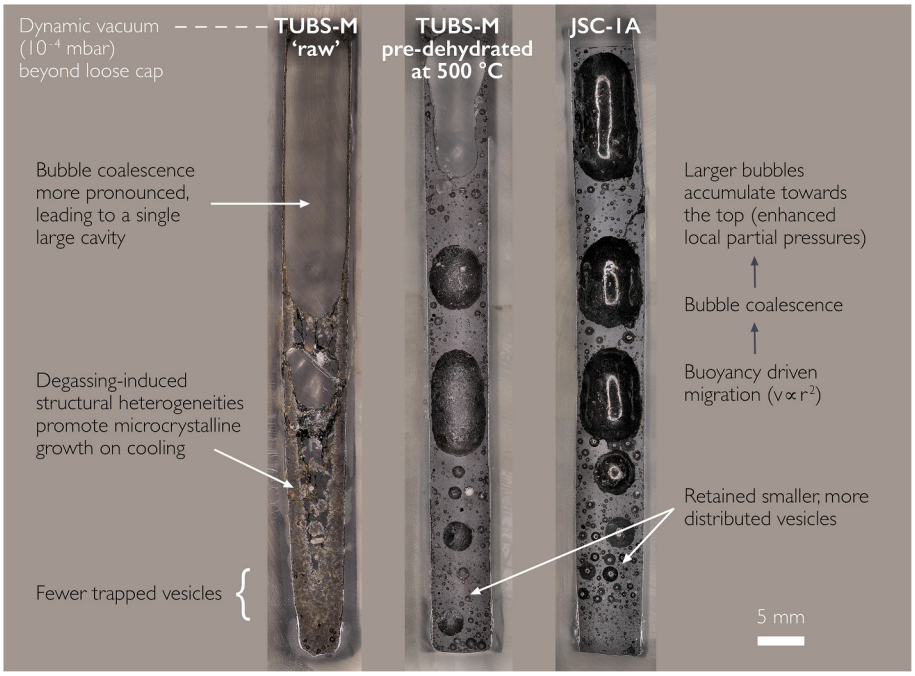

Fig. 10. Sample sections (set in resin) following NPD to 1120 °C, with cooling at 10 °C/min. Fewer trapped vesicles towards the base of the relatively volatile-enriched TUBS-M is potentially due to more efficient local bubble migration at lower initial viscosity, with melt compaction from the expanding upper void displacing deeper bubbles upwards. Apparent porosities may be exaggerated following densification upon partial melting, in tandem with sample migration up container walls (Dominguez and Whitlow, 2019), creating a natural central cavity (Fig. S2).

et al., 2017; Casas et al., 2023), whilst enhancing the solubility (Brooker et al., 2001) and diffusivity (Persikov et al., 2010) of volatiles contained therein.

Given the considerable advancement in melt progression within the larger TUBS-M volumes ca. 200–300 °C beyond the bulk of water release, overhead percolation distance will affect the sintering window for a certain composition and heating rate. Agitation suggestions (Lim et al., 2023) may not be practical for uncontained structures. If partial melting is engaged to enhance consolidation, the temperature window will coincide with the primary – lunar-like – mass loss for fresh samples around 1100 °C, just before or after the apparent solidus. The post-solidus contribution is independent of material weathering and limited to <0.06 wt% (up to 1300 °C) across the investigated samples, which falls short of actual lunar concentrations, notably in S. Sulfur in lunar regolith has a relatively minor effect on melt onset as the reduced forms do not strongly interact with the silicate network. An exception may be near Fe-FeS eutectic temperatures in Fe-rich regions, where troilite and other sulfide phases could promote localised early melting. The primary relevance of additional sulfur in lunar melting processes is rather in degassing and redox balance. The preference for less mobile carbon and sulfur species in terrestrial material might therefore inadvertently replicate aspects of lunar volatile behaviour, such as increased bubble density, despite the inherently more efficient degassing style associated with lunar species like CO, H_2S, or S_2.

4.5. Focusing pre-treatment

Efforts to reduce the bulk (up to 700–1000 °C) of volatiles in simulants are particularly encouraged for larger-scale studies due to primarily water-driven reaction influences, recognising freshness cannot be easily 'corrected' (i.e. processed Mauna Kea ash versus Kīlauea) and introduces new deviations, e.g. grain consolidation (Wilkerson et al., 2023) and residual oxides. Moreover, it is suspected that the surprising result in Fig. 7b arises because of structural defects or reactive sites created during partial dehydration that interact more effectively with the subsequently added soda-lime glass, leading to more extensive melting than when combined with the raw 'wetter' simulant. This outcome may be an unavoidable consequence of pre-treatment of partially glassy analogue material. Whilst 500 °C is sufficient to drive off the majority (81 %) of volatiles in TUBS-M without discernibly affecting particle size distribution, it would liberate less than half of that (38 %) in EAC-1A. The translational fluxing effect of this remnant water likely obscured the influence of glass content in the comparison of sintering temperatures between EAC-1A and JSC-1A in Ginés-Palomares et al. (2023).

A conscious pre-treatment of any designated lunar analogue should consider the envisaged thermal strategy, as well as sample individuality. For furnace heating where particular viscosities may be targeted, long and elevated pre-heating is advised. Occasional sample turnover would help liberate exsolved volatiles at depths beyond a few cm. Volume-appropriate time scales should be further investigated. Exceeding T_C is not critical as temperatures are too low for stable consolidation and would be experimentally surpassed. Sample loading would benefit from being performed within a vacuum chamber, if practical, to limit trapped intergranular air. Similarly, if the aim is to evaluate the cooled product of rapid (laser, microwave) beam heating, this approach would reduce porosity from terrestrial contamination at the expense of particle agglomeration. However, pre-treatment temperatures should be more conservative (below sintering) under this setup when investigating melting parameter refinement, whereupon strict grain distribution is sought. Therefore, although naturally-sourced terrestrial material cannot be an effective proxy in replicating complete thermal treatment of lunar regolith, simulants and fresher samples are best applied to isolate the effects of particular processing stages.

5. Conclusions

Regolith from the ancient mare basins is better approximated by younger volcanic material uncompromised by terrestrial alteration. With the exception of JSC-1A, the simulants catalogued here exhibit higher volatile degassing than freshly collected samples below solidus temperatures. Differences with the lunar regolith can be divided by this

threshold. Excess terrestrial H_2O, and to a lesser extent CO_2, act as depressants of melt onset. The fluxing effect of these partial pressures and degassing (in)efficiency is exacerbated at scale from impeded gas percolation; heating timescales are relevant for all pre-treatment and melting strategies and require further exploration at different sample volumes. When water and carbonate content is minimised, analogue fidelity is limited by the volatiles inherent to the melt. Above the solidus, elevated lunar sulfur and carbon contents primarily promote more abundant and efficient bubble formation. Unless fresher sources become widely distributed, sintering and melting experiments with different simulant compositions will rely on more deliberate pre-treatment strategies at typically higher temperatures than previously conducted. Temperature ranges and features reported herein to assist this targeting relate to a dry nitrogen atmosphere at a given rate. Using analogue or even returned samples to predict degassing behaviour under lunar surface conditions is challenged by the reproducibility of lunar vacuum, low gravity, and strongly reducing conditions. These environmental factors could further influence degassing kinetics, melt viscosity, bubble coalescence/migration, and crystallisation pathways. Going forward, it is not unreasonable that smaller quantities of oxides could be manipulated under controlled redox states to synthesise more realistic-performing crystalline material for validating melt processing strategies.

CRediT authorship contribution statement

Jennifer Sutherland: Writing – original draft, Visualization, Validation, Software, Methodology, Investigation, Formal analysis, Conceptualization. **Kai-Uwe Hess:** Writing – review & editing, Validation, Supervision, Resources, Methodology, Investigation, Formal analysis, Conceptualization. **Thilo Bissbort:** Writing – review & editing, Formal analysis. **Simon Stapperfend:** Writing – review & editing, Resources, Investigation. **Axel Müller:** Supervision, Project administration, Funding acquisition. **Thomas C. Hansen:** Writing – review & editing, Supervision, Methodology, Investigation, Data curation. **Alexander Rack:** Investigation, Data curation. **Donald B. Dingwell:** Writing – review & editing, Supervision, Resources, Project administration, Funding acquisition, Conceptualization.

Declaration of competing interest

The authors declare that they have no known competing financial interests or personal relationships that could have appeared to influence the work reported in this paper.

Acknowledgements

J.S. has received funding from Marie Skłodowska-Curie Actions under grant agreement No. 847439 (InnovaXN). D.B.D. wishes to acknowledge the support and infrastructural funding of the ERC 2018 ADV Grant 834225 (EAVESDROP). Volcanic samples were kindly supplied by John Hamilton (University of Hawai'i at Hilo), Ulrich Küppers (LMU), and Fabian Wadsworth (Durham University). Beam time for this study was provided by the Institut Laue-Langevin (5-24-712 and INTER-561) and the European Synchrotron Radiation Facility (ES-1303); special thanks go to Romain Garlet and Yves Watier for custom-building the induction furnace at the ESRF. The assistance of Graciela Díaz de Delgado, Analio Dugarte-Dugarte, and Tom Blanton in accessing the ICDD PDF-5+ database to support mineral identification was gratefully received. We thank Dirk Müller (LMU) for insights on the phase assemblage of simulants.

Appendix A. Supplementary data

Supplementary data to this article can be found online at https://doi.org/10.1016/j.chemgeo.2025.123115.

Data availability

Data will be made available on request.

References

Anderson, A.T., Brown, G.G., 1993. CO_2 contents and formation pressures of some Kilauean melt inclusions. Am. Mineral. 78 (7–8), 794–803.
Brooker, R.A., Kohn, S.C., Holloway, J.R., McMillan, P.F., 2001. Structural controls on the solubility of CO_2 in silicate melts: part I: bulk solubility data. Chem. Geol. 174 (1–3), 225–239. https://doi.org/10.1016/S0009-2541(00)00353-3.
Burnham, C.W., 1979. The importance of volatile constituents. In: Yoder, H.S. (Ed.), The Evolution of the Igneous Rocks. Princeton University Press, pp. 439–482.
Burton, M., Aiuppa, A., Allard, P., Asensio-Ramos, M., Cofrades, A.P., La Spina, A., et al., 2023. Exceptional eruptive CO_2 emissions from intra-plate alkaline magmatism in the Canary volcanic archipelago. Commun. Earth Environ. 4 (1), 467. https://doi.org/10.1038/s43247-023-01103-x.
Caprio, L., Demir, A.G., Previtali, B., Colosimo, B.M., 2020. Determining the feasible conditions for processing lunar regolith simulant via laser powder bed fusion. Addit. Manuf. 32, 101029. https://doi.org/10.1016/j.addma.2019.101029.
Casas, A.S., Hess, K.U., Badro, J., Eitel, M., Dingwell, D.B., 2023. A redox effect on the viscosity of molten pyrolite. Chem. Geol. 642, 121816. https://doi.org/10.1016/j.chemgeo.2023.121816.
Chen, X., Zhang, Y., Hui, D., Chen, M., Wu, Z., 2017. Study of melting properties of basalt based on their mineral components. Compos. Part B Eng. 116, 53–60. https://doi.org/10.1016/j.compositesb.2017.02.014.
Clark, D., Keller, B., Kirkland, J., 2009. Field test results of the PILOT hydrogen reduction reactor. In: AIAA Space 2009 Conference and Exposition. https://doi.org/10.2514/6.2009-6475.
Collins, P.J., Edmunson, J., Fiske, M., Radlińska, A., 2022. Materials characterization of various lunar regolith simulants for use in geopolymer lunar concrete. Adv. Space Res. 69 (11), 3941–3951. https://doi.org/10.1016/j.asr.2022.03.012.
Di Genova, D., Vasseur, J., Hess, K.U., Neuville, D.R., Dingwell, D.B., 2017. Effect of oxygen fugacity on the glass transition, viscosity and structure of silica-and iron-rich magmatic melts. J. Non-Cryst. Solids 470, 78–85. https://doi.org/10.1016/j.jnoncrysol.2017.05.013.
Dingwell, D.B., 1991. Redox viscometry of some Fe-bearing silicate melts. Am. Mineral. 76 (9–10), 1560–1562.
Dingwell, D.B., 1998. The glass transition in hydrous granitic melts. Phys. Earth Planet. Inter. 107 (1–3), 1–8. https://doi.org/10.1016/S0031-9201(97)00119-2.
Dingwell, D.B., Romano, C., Hess, K.U., 1996. The effect of water on the viscosity of a haplogranitic melt under PTX conditions relevant to silicic volcanism. Contrib. Mineral. Petrol. 124 (1), 19–28. https://doi.org/10.1007/s004100050170.
Dominguez, J.A., Whitlow, J., 2019. Upwards migration phenomenon on molten lunar regolith: New challenges and prospects for ISRU. Adv. Space Res. 63 (7), 2220–2228. https://doi.org/10.1016/j.asr.2018.12.014.
Dottin, J.W., Farquhar, J., Kim, S.T., Shearer, C., Wing, B., Sun, J., Ni, P., 2022. Isotopic evidence of sulfur photochemistry during lunar regolith formation. Geochem. Perspect. Lett. 23. https://doi.org/10.7185/geochemlet.2235.
Duffield, W., Riggs, N., Kaufman, D., Champion, D., Fenton, C., Forman, S., McIntosh, W., Hereford, R., Plescia, J., Ort, M., 2006. Multiple constraints on the age of a Pleistocene lava dam across the Little Colorado River at Grand Falls, Arizona. Geol. Soc. Am. Bull. 118 (3–4), 421–429. https://doi.org/10.1130/B25814.1.
Engelschiøn, V.S., Eriksson, S.R., Cowley, A., Fateri, M., Meurisse, A., Kueppers, U., Sperl, M., 2020. EAC-1A: A novel large-volume lunar regolith simulant. Sci. Rep. 10 (1), 5473. https://doi.org/10.1038/s41598-020-62312-4.
Epstein, S., Taylor Jr., H.P., 1973. The isotopic composition and concentration of water, hydrogen, and carbon in some Apollo 15 and 16 soils and in the Apollo 17 orange soil. Proc. Fourth Lunar Sci. Conf. 1559–1575.
Epstein, S., Taylor Jr., H.P., 1974. D/H and $^{18}O/^{16}O$ ratios of H_2O in the 'rusty' breccia 66095 and the origin of 'lunar water'. Proc. Fifth Lunar Sci. Conf. 1839–1854.
Farries, K.W., Visintin, P., Smith, S.T., van Eyk, P., 2021. Sintered or melted regolith for lunar construction: state-of-the-art review and future research directions. Constr. Build. Mater. 296, 123627. https://doi.org/10.1016/j.conbuildmat.2021.123627.
Fateri, M., Sottong, R., Kolbe, M., Gamer, J., Sperl, M., Cowley, A., 2019. Thermal properties of processed lunar regolith simulant. Int. J. Appl. Ceram. Technol. 16 (6), 2419–2428. https://doi.org/10.1111/ijac.13267.
Fegley, B., Swindle, T.D., 1993. Lunar volatiles: implications for lunar resource utilization. In: Lewis, J.S., Mathews, M.S., Guerrieri, L. (Eds.), Resources of Near-Earth Space. University of Arizona Press, Tucson.
Gallagher, P.K., Johnson, D.W., Schrey, F., 1970. Thermal decomposition of iron (II) sulfates. J. Am. Ceram. Soc. 53 (12), 666–670. https://doi.org/10.1111/j.1151-2916.1970.tb12038.x.
Gazulla, M.F., Gómez, M.P., Orduña, M., Zumaquero, E., Vicente, S., 2009. Sulfur determination in geological samples based on coupled analytical techniques: Electric furnace-IC and TGA-EGA. Geostand. Geoanal. Res. 33 (1), 71–84. https://doi.org/10.1111/j.1751-908X.2008.00902.x.
Giammaria, G., Lefferts, L., 2019. Catalytic effect of water on calcium carbonate decomposition. J CO_2 Util 33, 341–356. https://doi.org/10.1016/j.jcou.2019.06.017.
Gibson, E.K., 1977. Volatile elements, carbon, nitrogen, sulfur, sodium, potassium and rubidium in the lunar regolith. Phys. Chem. Earth 10 (C), 57–62. https://doi.org/10.1016/0079-1946(77)90006-4.

Gibson, E.K., Johnson, S., 1971. Thermal analysis-inorganic gas release studies of lunar samples. Proc. Second Lunar Sci. Conf. 1351–1366.
Gibson, E.K., Brett, R., Andrawes, F., 1977. Sulfur in lunar mare basalts as a function of bulk composition. Proc. Eighth Lunar Science Conf. 1417–1428.
Ginés-Palomares, J.C., Fateri, M., Schubert, T., de Peindray d'Ambelle, L., Simon, S., Gluth, G.J., Zocca, A., 2023. Material aspects of sintering of EAC-1A lunar regolith simulant. Sci. Rep. 13 (1), 23053. https://doi.org/10.1038/s41598-023-50391-y.
Giuliani, L., Iezzi, G., Hippeli, T., Davis, M., Elbrecht, A., Vetere, F., et al., 2020. The onset and solidification path of a basaltic melt by in situ differential scanning calorimetry (DSC) and ex situ investigations. Front. Earth Sci. 8, 337. https://doi.org/10.3389/feart.2020.00337.
Guerrero-Gonzalez, F.J., Zabel, P., 2023. System analysis of an ISRU production plant: Extraction of metals and oxygen from lunar regolith. Acta Astronaut. 203, 187–201. https://doi.org/10.1016/j.actaastro.2022.11.050.
Han, W., Zhou, Y., Cai, L., Zhou, C., Ding, L., 2024. Physical, mechanical and thermal properties of vacuum sintered HUST-1 lunar regolith simulant. Int. J. Min. Sci. Technol. 34 (9), 1243–1257. https://doi.org/10.1016/j.ijmst.2024.06.004.
Haskin, L.A., Warren, P.H., 1991. Lunar Chemistry. In: Heiken, G.H., Vaniman, D.T., French, B.M. (Eds.), Lunar Sourcebook: A Users Guide to the Moon. Cambridge University Press.
Hauri, E.H., Saal, A.E., Rutherford, M.J., Van Orman, J.A., 2015. Water in the Moon's interior: Truth and consequences. Earth Planet. Sci. Lett. 409, 252–264. https://doi.org/10.1016/j.epsl.2014.10.053.
Holtz, F., Behrens, H., Dingwell, D.B., Johannes, W., 1995. H_2O solubility in haplogranitic melts: compositional, pressure, and temperature dependence. Am. Mineral. 80 (1–2), 94–108.
Hu, G., Dam-Johansen, K., Wedel, S., Hansen, J.P., 2006. Decomposition and oxidation of pyrite. Prog. Energy Combust. Sci. 32 (3), 295–314. https://doi.org/10.1016/j.pecs.2005.11.004.
Hurley, D.M., Siegler, M.A., Cahill, J.T., Colaprete, A., Costello, E., Deutsch, A.N., Schaible, M., 2023. Surface volatiles on the Moon. Rev. Mineral. Geochem. 89 (1), 787–827. https://doi.org/10.2138/rmg.2023.89.18.
Jagota, A., Mikeska, K.R., Bordia, R.K., 1990. Isotropic Constitutive Model for Sintering Particle Packings. J. Am. Ceram. Soc. 73 (8), 2266–2273. https://doi.org/10.1111/j.1151-2916.1990.tb07587.x.
John, K.K., Rogers, C.E., 2021. Classifications and Requirements for Testing Systems and Hardware to Be Exposed to Dust in Planetary Environments (No. NASA-STD-1008). National Aeronautics and Space Administration.
Johnson, M.C., Anderson, A.T., Rutherford, M.J., 1994. Pre-eruptive volatile contents of magmas. Rev. Mineral. Geochem. 30 (1), 281–330. https://doi.org/10.1515/9781501509674-014.
Koch, L., Schmidt, B.C., 2023. CO_2 diffusion in dry and hydrous leucititic melt. Eur. J. Mineral. 35 (1), 117–132. https://doi.org/10.5194/ejm-35-117-2023.
Kotra, R.K., Gibson, E.K., Urbancic, M.A., 1982. Release of volatiles from possible Martian analogs. Icarus 51 (3), 593–605. https://doi.org/10.1016/0019-1035(82)90148-8.
La Spina, G., Arzilli, F., Burton, M.R., Polacci, M., Clarke, A.B., 2022. Role of volatiles in highly explosive basaltic eruptions. Commun. Earth Environ. 3 (1), 156. https://doi.org/10.1038/s43247-022-00479-6.
Lawrence, D.J., Peplowski, P.N., Wilson, J.T., Elphic, R.C., 2022. Global hydrogen abundances on the lunar surface. J. Geophys. Res. Planets 127 (7). https://doi.org/10.1029/2022JE007197 e2022JE007197.
Li, S., Milliken, R.E., 2017. Water on the surface of the Moon as seen by the Moon Mineralogy Mapper: distribution, abundance, and origins. Sci. Adv. 3 (9). https://doi.org/10.1126/sciadv.1701471.
Lim, S., Degli-Alessandrini, G., Bowen, J., Anand, M., Cowley, A., 2023. The microstructure and mechanical properties of microwave-heated lunar simulants at different input powers under vacuum. Sci. Rep. 13 (1), 1–14. https://doi.org/10.1038/s41598-023-29030-z.
Lin, H., Li, S., Xu, R., Liu, Y., Wu, X., Yang, W., Wang, C., 2022. In situ detection of water on the Moon by the Chang'E-5 lander. Sci. Adv. 8 (1). https://doi.org/10.1126/sciadv.abl9174.
Lin, H., Xu, R., Li, S., Chang, R., Hui, H., Liu, Y., et al., 2024. Higher water content observed in smaller size fraction of Chang'e-5 lunar regolith samples. Sci. Bull. https://doi.org/10.1016/j.scib.2024.05.031.
Linke, S., Windisch, L., Kueter, N., Wanvik, J.E., Voss, A., Stoll, E., Kwade, A., 2020. TUBS-M and TUBS-T based modular Regolith Simulant System for the support of lunar ISRU activities. Planet. Space Sci. 180, 104747. https://doi.org/10.1016/j.pss.2019.104747.
Liu, Y., Guan, Y., Zhang, Y., Rossman, G.R., Eiler, J.M., Taylor, L.A., 2012. Direct measurement of hydroxyl in the lunar regolith and the origin of lunar surface water. Nat. Geosci. 5 (11), 779–782. https://doi.org/10.1038/ngeo1601.
Long-Fox, J.M., Landsman, Z.A., Easter, P.B., Millwater, C.A., Britt, D.T., 2023. Geomechanical properties of lunar regolith simulants LHS-1 and LMS-1. Adv. Space Res. 71 (12), 5400–5412. https://doi.org/10.1016/j.asr.2023.02.034.
Martin, A., Wagoner, C., 2022. JHU-APL LSII Report: 2022 Lunar Simulant Assessment. Lunar Surface Innovation Consortium.
McCubbin, F.M., Kaaden, K.E.V., Tartèse, R., Klima, R.L., Liu, Y., Mortimer, J., et al., 2015. Magmatic volatiles (H, C, N, F, S, Cl) in the lunar mantle, crust, and regolith: Abundances, distributions, processes, and reservoirs. Am. Mineral. 100 (8–9), 1668–1707. https://doi.org/10.2138/am-2015-4934ccbyncnd.
McKay, D.S., Heiken, G., Basu, A., Blanford, G., Simon, S., Reedy, R., Papike, J., 1991. The Lunar Regolith. In: Heiken, G.H., Vaniman, D.T., French, B.M. (Eds.), Lunar Sourcebook: A Users Guide to the Moon. Cambridge University Press.
Metrich, N., Clocchiatti, R., 1996. Sulfur abundance and its speciation in oxidized alkaline melts. Geochim. Cosmochim. Acta 60 (21), 4151–4160. https://doi.org/10.1016/S0016-7037(96)00229-3.
Meyer, C., 2004. Lunar Sample Compendium: Samples 15425-15427; 15365-15377. Lunar Planetary Inst. https://www.lpi.usra.edu/lunar/samples/atlas/compendium/15425.pdf.
Meyer, C., 2010. Lunar Sample Compendium: Sample 74220. Lunar Planetary Inst. https://www.lpi.usra.edu/lunar/samples/atlas/compendium/74220.pdf.
Milliken, R.E., Li, S., 2017. Remote detection of widespread indigenous water in lunar pyroclastic deposits. Nat. Geosci. 10 (8), 561–565. https://doi.org/10.1038/ngeo2993.
Moore, C.B., Lewis, C.F., Gibson, E.K., Nichiporuk, W., 1970. Total carbon and nitrogen abundances in lunar samples. Science 167 (3918), 495–497. https://doi.org/10.1126/science.167.3918.495.
Morrison, A.A., Zanetti, M., Hamilton, C.W., Lev, E., Neish, C.D., Whittington, A.G., 2019. Rheological investigation of lunar highland and mare impact melt simulants. Icarus 317, 307–323. https://doi.org/10.1016/j.icarus.2018.08.001.
Mortimer, J., Verchovsky, A.B., Anand, M., Gilmour, I., Pillinger, C.T., 2015. Simultaneous analysis of abundance and isotopic composition of nitrogen, carbon, and noble gases in lunar basalts: Insights into interior and surface processes on the Moon. Icarus 255, 3–17. https://doi.org/10.1016/j.icarus.2014.10.006.
Mysen, B.O., 1976. The role of volatiles in silicate melts; solubility of carbon dioxide and water in feldspar, pyroxene, and feldspathoid melts to 30 kb and 1625 °C. Am. J. Sci. 276 (8), 969–996.
NASA, 2007. JSC-1A: Characterization summary of JSC-1A bulk lunar mare regolith simulant. https://ares.jsc.nasa.gov/projects/simulants/attachments/JSC-1A_Bulk_Data_Characterization_draft.pdf.
Ni, H., Keppler, H., 2013. Carbon in silicate melts. Rev. Mineral. Geochem. 75 (1), 251–287. https://doi.org/10.2138/rmg.2013.75.9.
Off Planet Research, 2025. Simulants, Feedstocks, and Additives. https://www.offplanetresearch.com/simulants-feedstocks-and-additives. Accessed: 27 March 2025.
Patridge, A.M., Whittington, A.G., Edmunson, J., 2025. The glass content of highland regolith simulants measured via high-temperature differential scanning calorimetry. In: 56th Lunar and Planetary Science Conference (Abstract No. 1364).
Persikov, E.S., Newman, S., Bukhtiyarov, P.G., Nekrasov, A.N., Stolper, E.M., 2010. Experimental study of water diffusion in haplobasaltic and haploandesitic melts. Chem. Geol. 276 (3–4), 241–256. https://doi.org/10.1016/j.chemgeo.2010.06.010.
Petkov, M.P., Voecks, G.E., 2023. Characterization of volatiles evolved during vacuum sintering of lunar regolith simulants. Ceram. Int. 49 (21), 33459–33468. https://doi.org/10.1016/j.ceramint.2023.06.178.
Petkov, M.P., Wilkerson, R.P., Voecks, G.E., Rickman, D.L., Edmunson, J.E., Effinger, M.R., 2024. Comparison of volatiles evolving from selected highland and mare lunar regolith simulants during vacuum sintering. Planet. Space Sci. 252, 105982. https://doi.org/10.1016/j.pss.2024.105982.
Ray, C.S., Reis, S.T., Sen, S., O'Dell, J.S., 2010. JSC-1A lunar soil simulant: Characterization, glass formation, and selected glass properties. J. Non-Cryst. Solids 356 (44–49), 2369–2374. https://doi.org/10.1016/j.jnoncrysol.2010.04.049.
Rees, C.E., Thode, H.G., 1974. Sulfur concentrations and isotope ratios in Apollo 16 and 17 samples. Proc. Fifth Lunar Sci. Conf. 1963–1973.
Reiss, P., Kerscher, F., Grill, L., 2020. Thermogravimetric analysis of chemical reduction processes to produce oxygen from lunar regolith. Planet. Space Sci. 181, 104795. https://doi.org/10.1016/j.pss.2019.104795.
Renggli, C.J., Steenstra, E.S., Saal, A.E., 2024. Sulfur in the Moon and Mercury. arXiv preprint arXiv:2410.18599.
Rutherford, M.J., Papale, P., 2009. Origin of basalt fire-fountain eruptions on Earth versus the Moon. Geology 37 (3), 219–222. https://doi.org/10.1130/G25402A.1.
Saal, A.E., Hauri, E.H., 2021. Large sulfur isotope fractionation in lunar volcanic glasses reveals the magmatic differentiation and degassing of the Moon. Sci. Adv. 7 (9), eabe4641. https://doi.org/10.1126/sciadv.abe4641.
Saal, A.E., Hauri, E.H., Cascio, M., van Orman, J.A., Rutherford, M.C., Cooper, R.F., 2008. Volatile content of lunar volcanic glasses and the presence of water in the Moon's interior. Nature 454 (7201), 192–195. https://doi.org/10.1038/nature07047.
Schlüter, L., Cowley, A., 2020. Review of techniques for In-Situ oxygen extraction on the moon. Planet. Space Sci. 181, 104753. https://doi.org/10.1016/j.pss.2019.104753.
Schrader, C., Rickman, D., Mclemore, C., Fikes, J., Wilson, S., Stoeser, D., et al., 2008. Extant and extinct lunar regolith simulants: Modal analyses of NU-LHT-1M and-2m, OB-1, JSC-1, JSC-1A and-1AF, FJS-1, and MLS-1. In: Planetary and Terrestrial Mining Symposium..
Šeško, R., Lamboley, K., Cutard, T., Grill, L., Reiss, P., Cowley, A., 2024. Oxygen production by solar vapor-phase pyrolysis of lunar regolith simulant. Acta Astronaut. 224, 215–225. https://doi.org/10.1016/j.actaastro.2024.08.009.
Shearer, C.K., Borg, L.E., Gaddis, L.R., 2020. Lunar Basalts and Pyroclastic Deposits. Science and Resource treasures Delivered from the Moon's Interior. In: Lunar Surface Science Workshop, 2241 (Abstract No. 5018).
Slabic, A., Gruener, J.E., Kovtun, R.N., Rickman, D.L., Sibille, L., Oravec, H.A., Edmunson, J., Keprta, S., 2024. Lunar Regolith Simulant User's Guide: Revision A (No. NASA/TM-20240011783). National Aeronautics and Space Administration.
Song, L., Xu, J., Fan, S., Tang, H., Li, X., Liu, J., Duan, X., 2019. Vacuum sintered lunar regolith simulant: Pore-forming and thermal conductivity. Ceram. Int. 45 (3), 3627–3633. https://doi.org/10.1016/j.ceramint.2018.11.023.
Stapperfend, S., Dingwell, D.B., Hess, K.U., Sutherland, J., Müller, A., Müller, D., et al., 2024. Viscosity measurements of selected lunar regolith simulants. Am. Mineral. https://doi.org/10.2138/am-2023-9263.
Street Jr., K.W., Ray, C., Rickman, D., Scheiman, D.A., 2010. Thermal Properties of Lunar Regolith Simulants. In: Proceedings of the 12th International Conference on

Engineering, Science, Construction, and Operations in Challenging Environments, pp. 266–275. https://doi.org/10.1061/41096(366)28.
Sutherland, J., Hansen, T.C., Dingwell, D.B., Müller, A., Linke, S., 2021. Sintering process of lunar regolith simulants by time- and temperature-resolved NPD [Dataset]. Inst. Laue-Langevin. https://doi.org/10.5291/ILL-DATA.INTER-561.
Sutherland, J., Hansen, T.C., Dingwell, D.B., Müller, A., 2024. Dehydration tracking and effect of soda-lime glass beads on high temperature sintering evolution of lunar regolith simulants [Dataset]. Inst. Laue-Langevin. https://doi.org/10.5291/ILL-DATA.5-24-712.
Taylor, L.A., Meek, T.T., 2005. Microwave sintering of lunar soil: properties, theory, and practice. J. Aerosp. Eng. 18 (3), 188–196. https://doi.org/10.1061/(ASCE)0893-1321(2005)18:3(188).
Taylor, G.J., Warren, P., Ryder, G., Delano, J., Pieters, C., Lofgren, G., 1991. Lunar rocks. In: Heiken, G.H., Vaniman, D.T., French, B.M. (Eds.), Lunar Sourcebook: A Users Guide to the Moon. Cambridge University Press.
Taylor, L.A., Pieters, C.M., Britt, D., 2016. Evaluations of lunar regolith simulants. Planet. Space Sci. 126, 1–7. https://doi.org/10.1016/j.pss.2016.04.005.
Taylor, S.L., Jakus, A.E., Koube, K.D., Ibeh, A.J., Geisendorfer, N.R., Shah, R.N., Dunand, D.C., 2018. Sintering of micro-trusses created by extrusion-3D-printing of lunar regolith inks. Acta Astronaut. 143, 1–8. https://doi.org/10.1016/j.actaastro.2017.11.005.
ten Kate, I.L., Cardiff, E.H., Dworkin, J.P., Feng, S.H., Holmes, V., Malespin, C., Stern, J. G., Swindle, T.D., Glavin, D.P., 2010. VAPoR - Volatile Analysis by Pyrolysis of Regolith - an instrument for in situ detection of water, noble gases, and organics on the Moon. Planet. Space Sci. 58 (7–8), 1007–1017. https://doi.org/10.1016/j.pss.2010.03.006.
ten Kate, I.L., Armstrong, R., Bernhardt, B., Blumers, M., Craft, J., Boucher, D., et al., 2013. Mauna Kea, Hawaii, as an analog site for future planetary resource exploration: results from the 2010 ILSO-ISRU field-testing campaign. J. Aerosp. Eng. 26 (1), 183–196. https://doi.org/10.1061/(ASCE)AS.1943-5525.0000200.
Varnam, M., Hamilton, C.W., Aleinov, I., Barnes, J.J., 2024. Composition and speciation of volcanic volatiles on the Moon. Icarus 116009. https://doi.org/10.1016/j.icarus.2024.116009.
Vasseur, J., Wadsworth, F.B., Lavallée, Y., Dingwell, D.B., 2016. Dynamic elastic moduli during isotropic densification of initially granular media. Geophys. J. Int. 204 (3), 1721–1728. https://doi.org/10.1093/gji/ggv550.
Verchovsky, A.B., Anand, M., Barber, S., 2020a. Quantitative Evolved Gas Analysis of Apollo Lunar Soils. Eur. Lunar Symp.
Verchovsky, A.B., Anand, M., Barber, S.J., Sheridan, S., Morgan, G.H., 2020b. A quantitative evolved gas analysis for extra-terrestrial samples. Planet. Space Sci. 181, 104830. https://doi.org/10.1016/j.pss.2019.104830.
Wadsworth, F.B., Vasseur, J., Llewellin, E.W., Schauroth, J., Dobson, K.J., Scheu, B., Dingwell, D.B., 2016. Sintering of viscous droplets under surface tension. Proc. R. Soc. A Math. Phys. Eng. Sci. 472 (2188). https://doi.org/10.1098/rspa.2015.0780.
Wadsworth, F.B., Vasseur, J., Llewellin, E.W., Dingwell, D.B., 2017. Sintering of polydisperse viscous droplets. Phys. Rev. E 95 (3), 033114. https://doi.org/10.1103/physreve.95.033114.
Wadsworth, F.B., Vasseur, J., Llewellin, E.W., Dingwell, D.B., 2022. Hot sintering of melts, glasses and magmas. Rev. Mineral. Geochem. 87 (1), 801–840. https://doi.org/10.2138/rmg.2022.87.17.
Wallace, P., Carmichael, I.S., 1992. Sulfur in basaltic magmas. Geochimica et Cosmochimica Acta 56 (5), 1863–1874. https://doi.org/10.1016/0016-7037(92)90316-B.
Wang, B.-W., Zhang, Q.W., Chen, Y., Zhao, W., Liu, Y., Tang, G.Q., et al., 2024. Returned samples indicate volcanism on the Moon 120 million years ago. Science 385 (6713), 1077–1080. https://doi.org/10.1126/science.adk6635.
Whittington, A.G., Parsapoor, A., 2022. Lower cost Lunar Bricks: Energetics of Melting and Sintering Lunar Regolith Simulants. New Space 10 (2), 193–204. https://doi.org/10.1089/space.2021.0055.
Whittington, A.G., Morrison, A.A., Parsapoor, A., Patridge, A.M., 2023. Thermal and Rheological Properties of Lunar Simulants from Ambient to Molten to Glass. In: 54th Lunar and Planetary Science Conference, 2806 (Abstract No. 2811).
Wilkerson, R.P., Petkov, M.P., Voecks, G.E., Lynch, C.S., Shulman, H.S., Sundaramoorthy, S., Choudhury, A., Rickman, D.L., Effinger, M.R., 2023. Outgassing behavior and heat treatment optimization of JSC-1A lunar regolith simulant. Icarus 400, 115577. https://doi.org/10.1016/j.icarus.2023.115577.
Zhang, Y., Ni, H., 2010. Diffusion of H, C, and O components in silicate melts. Rev. Mineral. Geochem. 72 (1), 171–225. https://doi.org/10.2138/rmg.2010.72.5.
Zhou, C., Mo, B., Tang, H., Gu, Y., Li, X., Zhu, D., et al., 2024. Multiple sources of water preserved in impact glasses from Chang'e-5 lunar soil. Sci. Adv. 10 (19). https://doi.org/10.1126/sciadv.adl2413.